

Quantifying Atmospheric Parameter Ranges for Ambient Secondary Organic Aerosol Formation

William C. Porter, Jose L. Jimenez, and Kelley C. Barsanti*

Cite This: *ACS Earth Space Chem.* 2021, 5, 2380–2397

Read Online

ACCESS |



Metrics & More



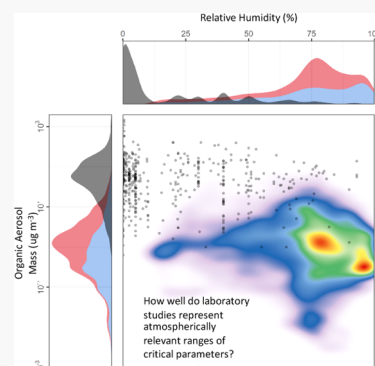
Article Recommendations



Supporting Information

ABSTRACT: Understanding of the fundamental chemical and physical processes that lead to the formation and evolution of secondary organic aerosol (SOA) in the atmosphere has been rapidly advancing over the past decades. Many of these advancements have been achieved through laboratory studies, particularly SOA studies conducted in environmental chambers. Results from such studies are used to develop simplified representations of SOA formation in regional- and global-scale air quality models. Although it is known that there are limitations in the extent to which laboratory experiments can represent the ambient atmosphere, there have been no systematic surveys of what defines atmospheric relevance in the context of SOA formation. In this work, GEOS-Chem version 12.3 was used to quantitatively describe atmospherically relevant ranges of chemical and meteorological parameters critical for predictions of the mass, composition, and physical properties of SOA. For some parameters, atmospherically relevant ranges are generally well represented in laboratory studies. However for other parameters, significant gaps exist between atmospherically relevant ranges and typical laboratory conditions. For example, cold winter (less than 0 °C) and humid (greater than 70% RH) conditions are relatively common on the Earth's surface but are poorly represented in published chamber data. Furthermore, the overlap in relative humidity and organic aerosol mass between chamber studies and ambient conditions is almost nonexistent. For parameters with significant gaps, extended laboratory studies and/or mechanistic models are needed to bridge these gaps.

KEYWORDS: secondary organic aerosol, nitrogen oxides, peroxy radicals, autoxidation, accretion, chamber studies, GEOS-Chem



INTRODUCTION

Organic aerosol (OA) makes up a significant fraction of submicron particle mass in the atmosphere¹ and thus adversely affects air quality and alters the Earth's radiative budget. OA includes primary organic aerosol (POA, directly emitted) and secondary organic aerosol (SOA, formed in situ). SOA can represent up to 65% of total OA mass in urban areas and 95% in remote areas.¹ Organic compounds with sufficiently low volatility to exist in the particle phase under ambient conditions contribute to SOA formation and growth; such compounds can be formed via gas-phase oxidation and/or multiphase reactions (e.g., accretion and organic salt formation).² In any given location, the extent of SOA formation is a function of (1) the identities and quantities of the precursors, (2) the reactivity of those precursors and their oxidation products, and (3) the tendencies of the oxidation and other reaction products to condense. All of these are in turn dependent on local meteorological and chemical conditions including temperature (T), relative humidity (RH), nitrogen oxides levels (NO_x), and oxidant levels [e.g., hydroxyl (OH), ozone (O_3), and nitrate (NO_3)].

SOA formation is highly dependent on gas-phase NO_x levels, and more precisely, the relative ratios of NO, hydroperoxyl radicals (HO_2), and peroxy radicals (RO_2).^{3–8} Volatile organic compounds (VOCs) react with atmospheric oxidants

to form RO_2 radicals. In stepwise sequential oxidation, bimolecular reactions of RO_2 with HO_2 , NO, and/or other RO_2 radicals (blue arrows Figure 1a) can lead to the formation of condensable products.^{9,10} The pathways that favor functionalization and production of lower volatility products promote SOA formation and growth. For example, it has been demonstrated that for aromatic compounds, SOA yields are lower under high NO conditions (dominant $\text{RO}_2 + \text{NO}$) due to greater formation of higher volatility organic nitrates and oxygenates, and SOA yields are higher under low NO conditions (dominant $\text{RO}_2 + \text{HO}_2/\text{RO}_2$) due to greater formation of lower volatility hydroperoxides, carboxylic acids, and hemiacetal oligomers.^{4,5,11} Historically, bimolecular $\text{RO}_2 + \text{RO}_2$ reactions have been thought to be relatively unimportant, and thus, the observed NO_x -dependence of SOA formation is often represented in models using a branching ratio (β) to calculate the fraction of VOC (as RO_2) that reacts with NO relative to HO_2 (Figure 1a, right panel);¹² each VOC fraction

Received: April 2, 2021
Revised: June 29, 2021
Accepted: June 29, 2021
Published: July 14, 2021



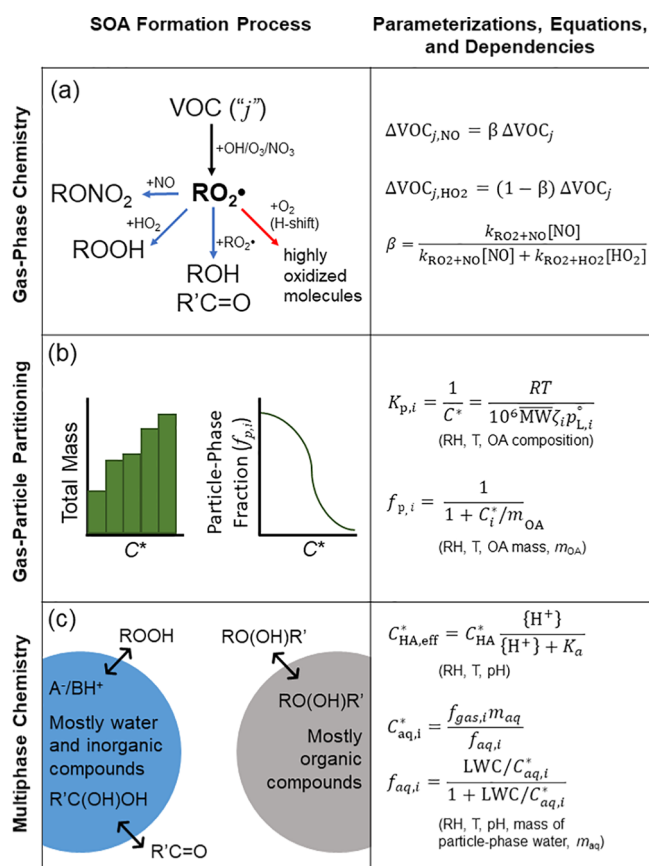


Figure 1. Schematic of relevant SOA formation processes: (a) gas-phase chemistry, (b) gas/particle partitioning, and (c) multiphase chemistry (left panels) and associated parameterizations, equations, and variables (right panels).

then has associated partitioning parameters that are typically derived from chamber studies.^{13,14} When RO_2 lifetimes are sufficiently long, intramolecular H-shift reactions can occur (RO_2 isomerization or autoxidation, as shown by a red arrow in Figure 1a).^{10,15,16} RO_2 isomerization reactions, particularly when occurring multiple times in sequence, can rapidly lower the vapor pressures of organic species by adding multiple oxygenated functional groups and producing compounds with higher oxygen to carbon (O/C) ratios than stepwise sequential oxidation.^{17,18} These highly oxidized molecules (“HOMs”) may also form dimers in the gas phase, further promoting SOA formation.^{18–20} The lack of data and detailed structure–activity relationships for autoxidation and RO_2 dimerization, and subsequent development of generalized parameterizations, has precluded the widespread inclusion of these processes in simplified representations of SOA formation.

The distribution of products formed from the oxidation, fragmentation, and functionalization of VOCs can be represented using the volatility basis set (VBS) approach, in which compounds are binned on a decadal scale based on their effective saturation vapor concentration, C^* (Figure 1b).²¹ The C^* value is the inverse of the gas/particle partitioning coefficient, K_p ($=1/C^*$), and facilitates an intuitive understanding of a compound’s general tendency to partition to the particle phase as the fraction of a compound in the particle phase, $f_p = 0.5$ when $C^* = m_{\text{OA}}$, where m_{OA} is the mass concentration of the absorbing OA phase (Figure 1b). The values of K_p (or C^*) are a function of vapor pressure, p_L° , and

composition of the absorbing organic phase.²² The composition of the absorbing phase determines the activity coefficient, ζ , of the condensing compound and mean molecular weight, MW , of the absorbing phase (Figure 1b).²² Values of p_L° , ζ , and MW are strongly influenced by T and RH; particularly when the presence of organic-phase water is considered, which modifies ζ and decreases the MW of the absorbing phase.^{23,24} The ζ values of organic compounds can be sufficiently high in particles with inorganic compounds and water to promote phase separation; phase separation can be predicted and parameterized as a function of RH and particle composition.^{25–27} Particle viscosity (and subsequently, molecular diffusion timescales) is also influenced by particle composition, T , and RH, such that under specific conditions (lower T and RH), the assumption of thermodynamic equilibrium is no longer valid, and a kinetic representation of gas/particle partitioning must be invoked.^{28–31}

In addition to SOA formation via condensation of oxidation products and HOM dimers formed in the gas phase, there are a number of multiphase SOA formation pathways that occur either in particles or on their surface (Figure 1c). Organic salt formation and accretion reactions are two examples of such pathways. The extent of organic salt formation can be parameterized using effective saturation concentrations for the participating acids ($C_{\text{HA,eff}}^*$) and bases ($C_{\text{B,eff}}^*$) that are dependent on particle pH (Figure 1c).^{2,32} Accretion reactions may occur in (on) largely organic and aqueous phases (particles); low molecular weight and highly soluble organic compounds are more likely to participate in aqueous-phase reactions.³³ For example, isoprene oxidation products with epoxide functionality partition to the aqueous phase and undergo acid-catalyzed ring opening followed by nucleophilic addition to form methyltetrols and organosulfates.^{34,35} Aqueous SOA formation pathways can be parameterized using an effective saturation concentration for the aqueous phase (C_{aq}^*), in which vapor pressure is replaced by effective Henry’s law constant, and m_{OA} by mass of particle-phase water (m_{aq}) or liquid water content (LWC).³⁶ These aqueous phase SOA formation pathways are highly dependent on particle pH and LWC.³⁷

In most widely used chemical transport models (CTMs), representation of SOA formation is parameterized using the two-product (2p) or VBS approach.^{21,38} In both approaches, chamber data are fit to obtain parameters that describe the molar yields (α) and gas/particle partitioning coefficients (K_p or C^*) of a finite number of products (2p) or bins (VBS) that are used to represent the suite of condensable reaction products. Parameters are typically derived using data from a series of experiments with a single VOC precursor + oxidant, under conditions designed to approach atmospheric relevance and minimize experimental artifacts.³⁹ Those parameters are then used to predict SOA formation from lumped model surrogates (e.g., high-yield aromatics, low-yield aromatics, and monoterpenes) under a range of ambient conditions. In this work, the global CTM GEOS-Chem was used to explore atmospherically relevant ranges of meteorological and chemical parameters critical for predictions of SOA mass, composition, and physical properties. Predicted values are discussed in the context of gas-phase chemistry, gas/particle partitioning, and multiphase chemistry relevant to SOA formation. Parameter ranges are discussed in the context of understanding the extent to which laboratory experimental data represent ambient

atmospheric conditions. Implications and opportunities for future experimental and modeling studies are also discussed.

Model Description. GEOS-Chem version 12.3 was used to provide modeled distributions of key meteorological and chemical parameters for SOA mass and composition in summer and winter months. Global $2^\circ \times 2.5^\circ$ simulations were performed for January and July 2013, including 1 month of discarded spinup, driven by the GEOS Forward Processing (GEOS-FP) operational data stream provided by the NASA Global Modeling and Assimilation Office (GMAO, <https://gmao.gsfc.nasa.gov>). GEOS-Chem was run using 47 hybrid σ -pressure levels ranging from the surface to 0.01 hPa; with upper atmosphere levels (beginning around 90 hPa) of the native 72-layer met product vertical grid lumped for computational efficiency.

Global anthropogenic emissions were from the Community Emissions Data System (CEDS),⁴⁰ supplemented by detailed regional inventories where available, including the United States (NEI11),⁴¹ Canada (CAC),⁴² East Asia (MIX),⁴³ and Africa (DICE-Africa).⁴⁴ Emissions from open fires were from the GFED4.1 inventory,⁴⁵ while lightning NO_x was parameterized to match region-specific climatological observations.⁴⁶ Biogenic emissions were included using the Model of Emissions of Gases and Aerosols from Nature (MEGAN v2.1)⁴⁷ with updates for acetaldehyde emissions⁴⁸ and CO_2 dependence.⁴⁹ Non-agricultural ammonia emissions were from the Global Emissions Initiative (GEIA) inventory (<http://www.geiacenter.org/>); online biogenic soil NO_x emissions were included following a study by Hudman et al.⁵⁰ Marine emissions of dimethyl sulfide (DMS),⁵¹ acetone,⁵² acetaldehyde,⁴⁸ and ammonia⁵³ also were included to supplement the global data sets.

Gas-phase chemistry was performed using the GEOS-Chem mechanism through the KPP chemical solver.⁵⁴ RO_2 bimolecular lifetime was calculated using gridded mixing ratios of 32 RO_2 species, tracked in this version of GEOS-Chem, and mixing ratios of NO and HO_2 ; $\text{RO}_2 + \text{RO}_2$ reactions were not considered in the RO_2 lifetime calculations. The bimolecular lifetime for each individual RO_2 species was determined based on summed pseudo-first-order reaction rates. The resultant RO_2 species-specific lifetimes were then averaged by grid cells (weighted by the RO_2 species mixing ratio) to obtain the gridded RO_2 lifetime.

Inorganic aerosol thermodynamics, including particle pH and LWC, were computed by the ISORROPIA II⁵⁵ module, as implemented by Pye et al.⁵⁶ Thus, LWC represents liquid water associated with the inorganic aerosol fraction only. SOA formation was modeled using the simplified VBS approach of Pye et al.¹³ with semi-volatile POA and SOA parameters for monoterpenes, sesquiterpenes, aromatics, alkanes, and intermediate VOCs, supplemented by the irreversible aqueous-phase isoprene and organonitrate SOA scheme of Marais et al.⁵⁷ Dry deposition was represented using the Wesely⁵⁸ “resistance-in-series” scheme, with aerosols handled following Zhang et al.⁵⁹ Wet deposition was included as described in Liu et al.⁶⁰ and Amos et al.⁶¹ for water soluble particles and gases, respectively, with Henry’s law constants as compiled by Sander et al.⁶² and Safieddine and Heald.⁶³

To examine the modeled distributions of meteorological and chemical parameters across multiple domains of interest, the output was subset both spatially and temporally. Vertical layers [surface, planetary boundary layer (PBL), and free troposphere] were defined for each grid cell using boundary heights,

as defined by the GEOS-FP product. Terrestrial distributions were determined by selecting only cells with a land fraction greater than zero; remaining cells were defined as oceanic. To differentiate areas with elevated OA levels, a concentration threshold of $0.5 \mu\text{g m}^{-3}$ was chosen for additional subsetting. Finally, population data from the Gridded Population of the World (GPWv4), a product of the Socioeconomic Data and Applications Center (SEDAC), were used to calculate all population-weighted statistical metrics.

Laboratory Data. Barsanti et al.³⁹ previously compiled a summary of SOA chamber data from 22 laboratory studies published between 1999 and 2011. With the exception of one foundational study that has been widely used to derive SOA parameterizations, data from those publications are not reported here. However, the data ranges reported by Barsanti et al.³⁹ are included in Table S1, and average T and RH values and the minimum and maximum m_{OA} values are included in the relevant figures.

Building on Barsanti et al.,³⁹ data were collected from 65 additional laboratory studies of SOA formation published between 1999 and 2018, with the majority of papers (49 of 65) published in 2012 or later. Only publications that reported SOA mass, or both reacted hydrocarbon (ΔHC) level and SOA yield (from which SOA mass could be calculated), were included. Temperature, RH, initial NO_x levels, and ΔHC levels were listed when reported or easily inferred; blanks indicate that no data were reported. While the majority of data were from batch experiments conducted in Teflon chambers, data were also included from stainless steel chambers (e.g., refs 64 and 65) and flow reactors (e.g., potential aerosol mass reactor).^{66,67} Experiments included single anthropogenic or biogenic precursors and mixtures (e.g., biogenic compound mixtures,⁶⁸ volatile chemical product mixtures,⁶⁹ and biomass burning emissions^{70,71}) under a wide range of conditions (i.e., differing oxidants, aging timescales, and UV spectra). The data and sources are summarized in Table S1.

RESULTS AND DISCUSSION

The GEOS-Chem model output parameters are presented in 15 figures in the main text and 17 figures in the Supporting Information; the figures are listed in Table 1 in order of appearance. They are presented as surface-level maps; terrestrial histograms shaded by OA mass threshold ($0.5 \mu\text{g m}^{-3}$); vertical mean box plots over land at the surface, within the PBL, and in the free troposphere; vertical mean box plots weighted by population density and filtered by the minimum OA mass threshold ($0.5 \mu\text{g m}^{-3}$); and vertical mean box plots over the ocean and filtered by the minimum OA mass threshold ($0.5 \mu\text{g m}^{-3}$). The ranges and means of all parameter values are listed in Table 2, sorted by general model confidence. The parameters are discussed in the context of gas-phase chemistry (oxidation pathways and radical fates: e.g., NO mixing ratio, β value, and RO_2 lifetime), the chemical and physical properties that influence gas/particle partitioning and multiphase chemistry (particle mass, composition, and phase: e.g., OA, T , RH, pH, and LWC), and the ranges for which relevant laboratory data are sparse to nonexistent (laboratory-model comparison: e.g., T and RH, RH and OA mass).

Oxidation Pathways and Radical Fates. The fate of RO_2 radicals is a key determinant in the volatility and functionality distributions of organic oxidation products formed in the atmosphere. In the context of SOA formation, research largely has been focused on the extent to which RO_2

Table 1. List of Figures in Manuscript and Supporting Information

Figure 1	relevant SOA formation processes, equations, and parameters	Figure S1	VOCs
Figure 2	NO	Figure S2	VOC/NO _x ratio
Figure 3	RO ₂ bimolecular branching ratio (β)	Figure S3	JNO ₂
Figure 4	RO ₂ bimolecular chemical lifetime	Figure S4	H ₂ O ₂ /HNO ₃
Figure 5	total OA	Figure S5	total RO ₂
Figure 6	temperature	Figure S6	organic fraction of PM _{2.5} mass
Figure 7	RH	Figure S7	SOA fraction of total organic mass
Figure 8	pH	Figure S8	total secondary inorganic aerosol (SIA)
Figure 9	particle LWC	Figure S9	total SOA
Figure 10	surface vs chamber NO _x and VOCs	Figure S10	biogenic SOA mass fraction
Figure 11	surface vs chamber conditions T and RH	Figure S11	anthropogenic SOA mass fraction
Figure 12	surface vs chamber conditions T and RH, high SOA formation potential	Figure S12	OM/OC
Figure 13	free troposphere vs chamber conditions T and RH	Figure S13	phase state (T_g/T)
Figure 14	number of studies with representative T and RH	Figure S14	SRH
Figure 15	surface vs chamber conditions RH and OA mass	Figure S15	phase separation (SRH/RH)
		Figure S16	surface vs chamber RH and OA mass, high SOA formation potential
		Figure S17	surface vs chamber NO _x and VOCs, high SOA formation potential

radicals react with NO versus HO₂, where reactions with NO are more prevalent under high NO_x conditions and with HO₂ under low NO_x conditions. To account for the observed dependence of SOA formation on NO_x conditions, the fraction of RO₂ radicals reacting with NO versus HO₂ has been parameterized in models as follows¹²

$$\beta = \frac{k_{\text{RO}_2+\text{NO}}[\text{NO}]}{k_{\text{RO}_2+\text{NO}}[\text{NO}] + k_{\text{RO}_2+\text{HO}_2}[\text{HO}_2]}$$

where $\beta = 1$ indicates that all of the RO₂ radicals react with NO. SOA formation is then predicted using a linear combination of SOA parameters derived from experiments in the absence of NO_x ($\beta \approx 0$) and presence of NO_x ($\beta \approx 1$). More recently, it has been demonstrated that unimolecular RO₂ reactions (H-shifts) leading to HOM formation are competitive for some RO₂ and that RO₂ dimerization can also occur; both types of reactions can contribute significantly to SOA formation. However, no generalized parameterizations exist for these processes, and thus, they are not included in most simplified representations of SOA formation in regional and global models.

Ambient NO emissions are associated with anthropogenic activities and thus are higher in urban or industrialized locations. Figure 2 shows that modeled NO values peak predictably over areas with the greatest human activity and population density (upper left), also resulting in strong hemispheric differences in mean surface levels. The monthly

mean distributions based on GEOS-Chem are heavy tailed (upper right) and reveal a correlation between higher OA concentrations (darker shaded bars) and higher NO levels, especially in the winter. Overall, monthly mean NO mixing ratios are less than 1 ppb across seasons and hemispheres, with a global terrestrial average of ~ 0.12 ppb.

Modeled mean summer β values (Figure 3) are roughly normal in distribution (greatest frequency between 0.25 and 0.75), with a downward shift during winter months, especially in more remote regions (Figure 3). Modeled β values also show a strong diurnal cycle in most locations, as indicated by the average daily maxima (~ 0.75) and minima ($\sim 0-0.12$) lines. Peak β values correspond to increasing NO in the daytime, especially in areas heavily impacted by anthropogenic emissions (average value ~ 0.5 over land surface), suggesting the importance of diurnal cycles for capturing the NO_x dependence of SOA formation. The wide distribution and strong diurnal cycle of modeled β values highlight a need for constraining β values in chamber studies and evaluating the extent to which linear combinations of existing SOA parameters adequately represent SOA formation across the range of atmospherically relevant conditions.

While the reactions of RO₂ with other RO₂ are thought to be a relatively minor pathway in the ambient atmosphere, recent research has demonstrated the potential importance of RO₂ unimolecular reactions (autoxidation) for atmospherically relevant systems. For bimolecular reactions with NO/HO₂, RO₂ lifetimes are on the order of 1 to 100 s. Reported unimolecular H-shift reaction rates are typically $< 1 \text{ s}^{-1}$.^{17,72} Thus, when RO₂ bimolecular lifetimes are on the order of 10 to 100 s, autoxidation may be competitive. Figure 4 shows the wide distribution of calculated monthly mean average RO₂ bimolecular lifetime (see Supporting Information for details). This qualitative assessment suggests that there are a number of regions over which unimolecular RO₂ reactions (autoxidation) may be competitive with bimolecular reactions. Furthermore, these regions with warmer temperatures and reduced NO emissions are expected to become increasingly common, even in many urban areas, increasing the potential importance of unimolecular RO₂ reactions (e.g., Praske et al.⁷³).

Particle Mass, Composition, and Phase State. As illustrated in Figure 1b, the fraction of any compound in the particle phase ($f_{p,i}$) increases non-linearly with an increase in OA mass (m_{OA}). Global modeled OA mass concentrations (Figure 5) show strong seasonality associated primarily with biogenic emissions. Distributions of monthly averages are heavy-tailed and span several orders of magnitude, from less than $1 \mu\text{g m}^{-3}$ to over $10 \mu\text{g m}^{-3}$. The ranges of values are largely consistent with the measured and modeled OA mass ranges reported by Spracklen et al.,⁷⁴ wherein OA mass was underpredicted in the base case simulation relative to the observations, as well as the modeled OA mass range of Tsigaridis et al.⁷⁵ The fractional contribution of SOA to total OA is shown in Figure S7, while the relative contributions of biogenic and anthropogenic SOA are shown in Figures S10 and S11, respectively.

Partitioning coefficients (C^*/K_p) are strongly dependent on temperature. For values derived at a given temperature (T^*), the temperature dependence in the ambient atmosphere can be represented assuming a constant ζ and \overline{MW} , as described by Sheehan and Bowman,⁷⁶ where the volatility of the lumped compound or model surrogate increases with T . In addition, at low T , particle viscosity increases, increasing the potential for

Table 2. Parameter Means and Standard Deviation for Surface, PBL, and UT; Sorted by General Confidence in the Parameter

description	units	model confidence	season	surface mean	surface std. dev.	PBL mean	PBL std. dev.	UT mean	UT std. dev.
temperature	°C	high	summer	19	9.38	17.1	8.53	-19.5	4.5
			winter	-1.4	19.8	-1.89	19.2	-28.5	4.7
RH	%	high	summer	67.1	20.2	67	19.5	58.6	16.1
			winter	72.8	22.1	72	22.7	54.2	17.8
JNO ₂ photolysis rate	1/s	high	summer	0.00344	0.00101	0.00367	0.000989	0.00604	0.000914
			winter	0.00134	0.00105	0.00142	0.00113	0.00249	0.00181
RO ₂ branching ratio	unitless	mid	summer	0.425	0.14	0.4	0.142	0.374	0.0624
			winter	0.336	0.18	0.3	0.166	0.191	0.104
total OA	μg/m ³	mid	summer	3.83	9.96	3.46	7.61	0.777	1.17
			winter	3.04	7.96	2.67	6.81	0.421	1.07
SOA: anthropogenic fraction	unitless	mid	summer	0.068	0.0962	0.0666	0.0904	0.0723	0.072
			winter	0.083	0.0889	0.0833	0.0857	0.0914	0.050
SOA: biogenic fraction	unitless	mid	summer	1.73	2.98	1.67	2.87	1.3	1.68
			winter	0.723	1.32	0.714	1.26	0.49	0.468
summed VOCs	ppbC	mid	summer	20.7	42	16.3	34.6	2.13	2.5
			winter	21.1	34	17.7	27.8	2.93	2.1
SOA vs summed VOCs	μg/m ³ /ppbC	mid	summer	0.29	0.487	0.331	0.506	0.349	0.388
			winter	0.053	0.0772	0.0624	0.0895	0.0765	0.0984
summed VOCs vs NO _x	ppbC/ppb	mid	summer	248	2010	322	2740	34.1	40.2
			winter	149	855	173	1070	114	165
secondary inorganic mass	μg/m ³	mid	summer	2.48	4.71	2.2	3.82	0.496	0.515
			winter	5.77	12.2	5.2	10.8	0.656	0.911
organic fraction PM _{2.5} mass	unitless	mid	summer	0.298	0.249	0.294	0.244	0.231	0.2
			winter	0.156	0.154	0.155	0.151	0.134	0.1
NO mixing ratio	ppb	mid	summer	0.0541	0.109	0.0372	0.0643	0.0277	0.015
			winter	0.176	0.971	0.129	0.677	0.0152	0.023
NO _x mixing ratio	ppb	mid	summer	0.616	1.2	0.342	0.599	0.0943	0.0625
			winter	1.42	2.9	0.992	2.19	0.0885	0.107
SOA mass	μg/m ³	mid	summer	1.84	1.9	1.73	1.7	0.359	0.261
			winter	0.868	1.8	0.793	1.6	0.133	0.215
[H ₂ O ₂]/[HNO ₃]	ppb/ppb	mid	summer	4.56	8.05	4.49	4.99	4.24	3.2
			winter	2.47	10.9	2.16	7.65	2.67	2.3
summed RO ₂ species (ppb)	ppb	mid	summer	0.0126	0.0104	0.0112	0.0079	0.00471	0.00118
			winter	0.00543	0.0106	0.00487	0.0081	0.00216	0.00166
RO ₂ lifetime	s	mid	summer	236	193				
			winter	16,400	73,800				

Table 2. continued

description	units	model confidence	season	surface mean	surface std. dev.	PBL mean	PBL std. dev.	UT mean	UT std. dev.
particle liquid water ($\mu\text{g}/\text{m}^3$)	$\mu\text{g}/\text{m}^3$	low	summer	5.4	12.5	4.07	8.47	0.847	1.04
			winter	22	44.4	19.9	40.4	1.85	2.43
particle pH	unitless	low	summer	1.07	0.82	0.968	0.772	-0.0428	0.565
			winter	1.35	1.1	1.24	1.06	-0.199	0.359
SOA fraction OA mass	unitless	low	summer	1.8	3.05	1.74	2.93	1.38	1.72
			winter	0.81	1.37	0.798	1.31	0.585	0.494
OM/OC from parent HC	OM/OC	very low	summer	2.04	0.142	2.05	0.136	2.06	0.117
			winter	1.96	0.159	1.97	0.153	2.04	0.0945
O/C ratio from binned SOA	O/C	very low	summer	0.699	0.113	0.704	0.109	0.714	0.0932
			winter	0.633	0.127	0.644	0.122	0.699	0.0756
separation RH	%	very low	summer	49.9	20.6	49	20	47.5	18.2
			winter	63.3	23.3	62	23	51.7	16.3
SRH vs RH (binned)	SRH/RH	very low	summer	0.806	0.359	0.78	0.341	0.861	0.344
			winter	0.932	0.474	0.91	0.411	1.03	0.405

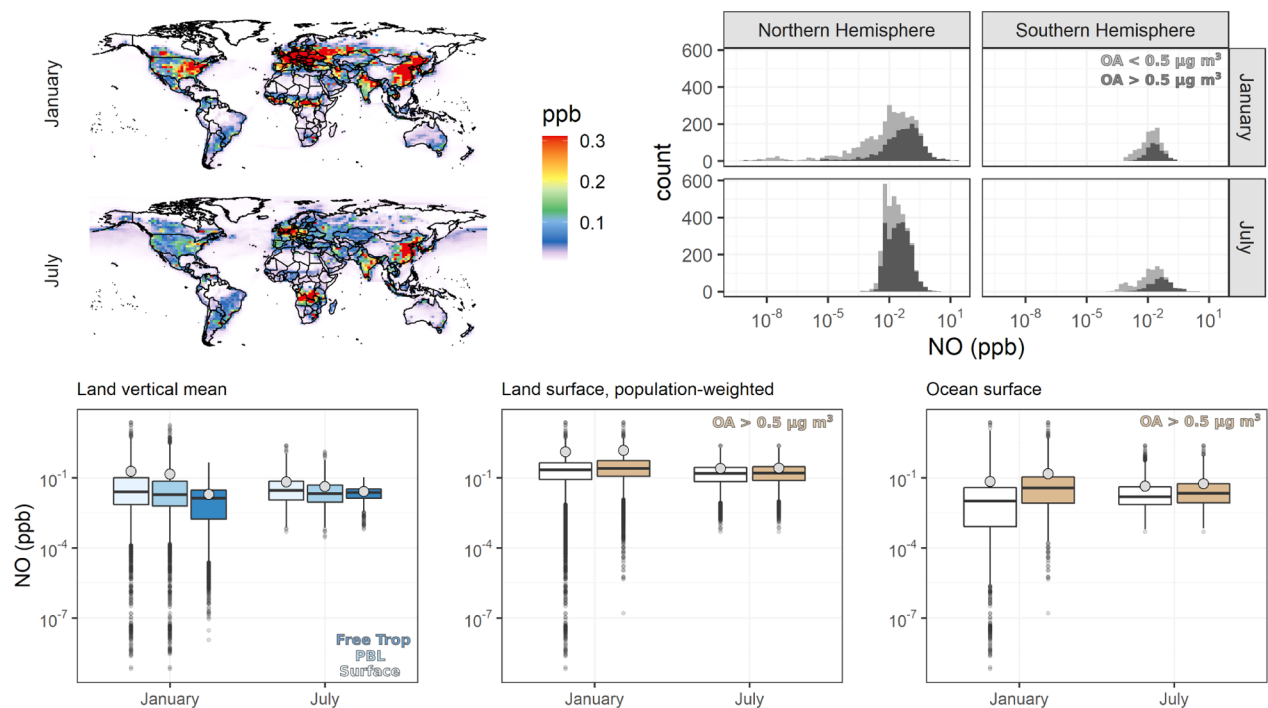


Figure 2. Monthly average NO for January and July 2013, presented as surface-level maps (upper left panel), land surface histograms (upper right panel), and subset box plots (lower panels). Histograms are shaded to differentiate regions averaging less than $0.5 \mu\text{g m}^{-3}$ OA by mass (light gray) from regions with at least that amount (dark gray), and exclude Antarctica. Land vertical mean box plots (lower left panel) show average values over land at the surface (light blue), within the PBL (blue), and within the free troposphere (dark blue). Population-weighted box plots (middle panel) show distributions weighted by gridded population density (white) and filtered for only cells showing an average of at least $0.5 \mu\text{g m}^{-3}$ OA by mass (brown). Ocean box plots (lower right) filter out all cells over land surfaces.

kinetic limitations to equilibrium gas/particle partitioning. Simulated global T distributions are shown in Figure 6. The broadest distribution in land surface temperature is observed in

the northern hemisphere, especially in the winter, due to the relative abundance of land mass at northern latitudes. The January land surface temperatures (excluding Antarctica) range

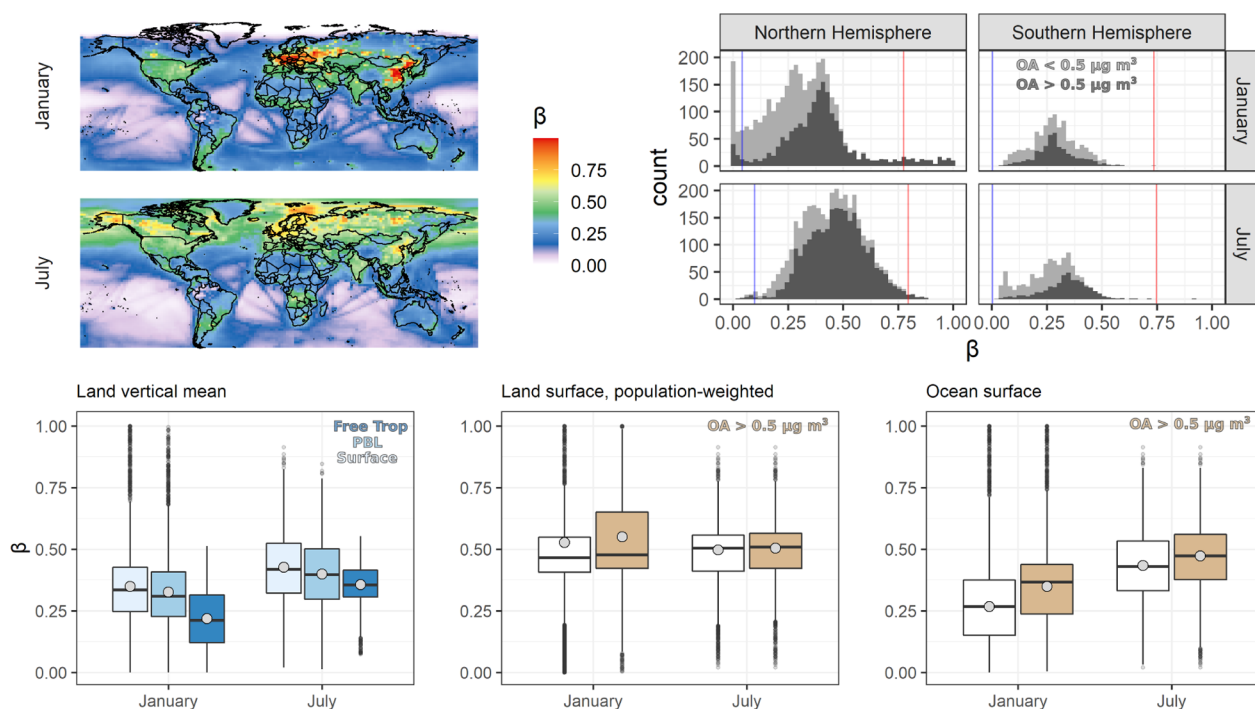


Figure 3. As with Figure 2, except for an average monthly bimolecular $\text{RO}_2 + \text{NO}/\text{HO}_2$ branching ratio. Histograms (upper right) also include average daily minimum (blue) and maximum values (red) based on hourly diurnal cycles for each season and hemisphere.

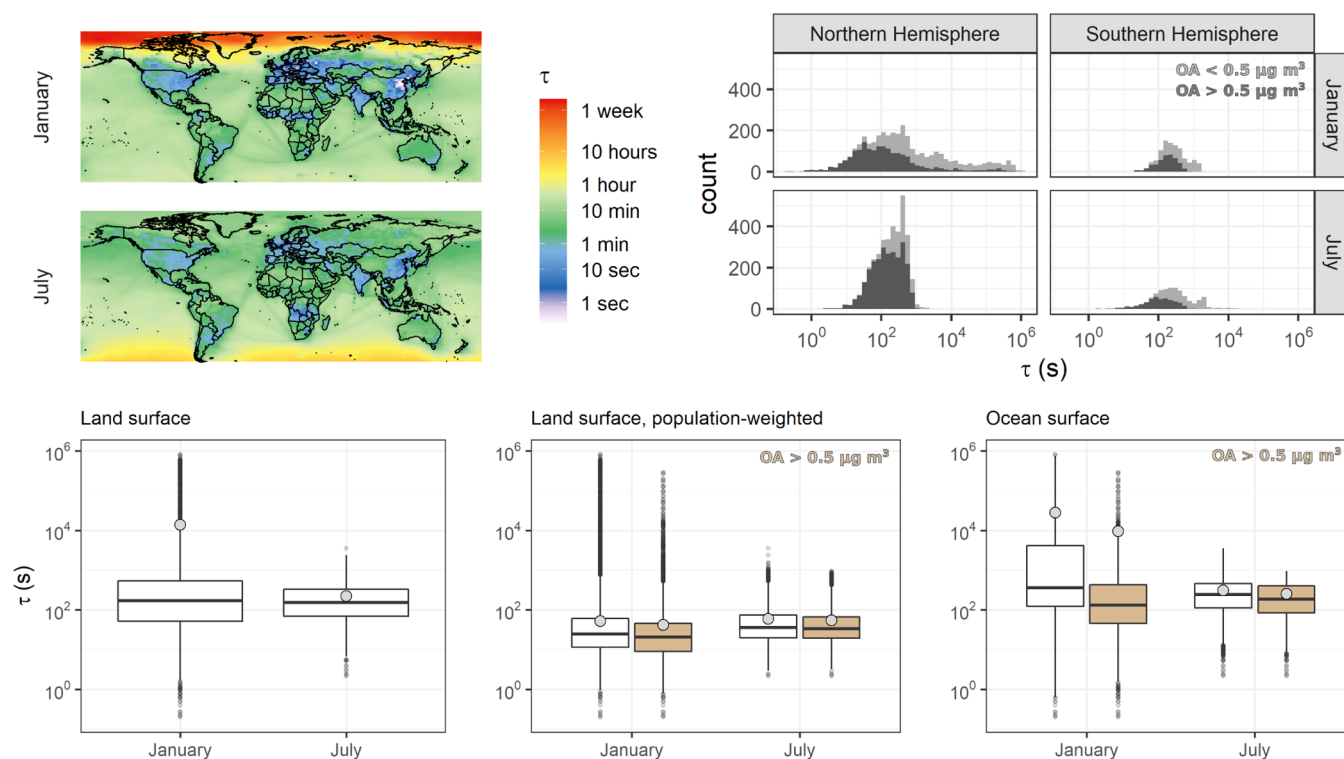


Figure 4. As with Figure 2, except for average monthly RO_2 bimolecular chemical lifetime.

from -20 to 20 °C (25th and 75th percentiles), with a monthly mean of 0 °C.

The distribution is significantly narrower in the northern hemisphere summer; the July land surface temperatures range from 12 to 25 °C (25th and 75th percentiles), with a monthly mean of 18 °C. Weighting these calculations by population reveals the human preference for living in above-freezing

conditions, shifting the mean temperature to around 12 °C for January and 25 °C for July. Ocean surface temperatures are milder than land surface, in general, showing reduced seasonality in both hemispheres due to a weaker temperature response to insolation. Masking temperature distributions by grid cells with elevated OA concentrations ($\text{OA} > 0.5 \mu\text{g m}^{-3}$) has little impact on the distributions.

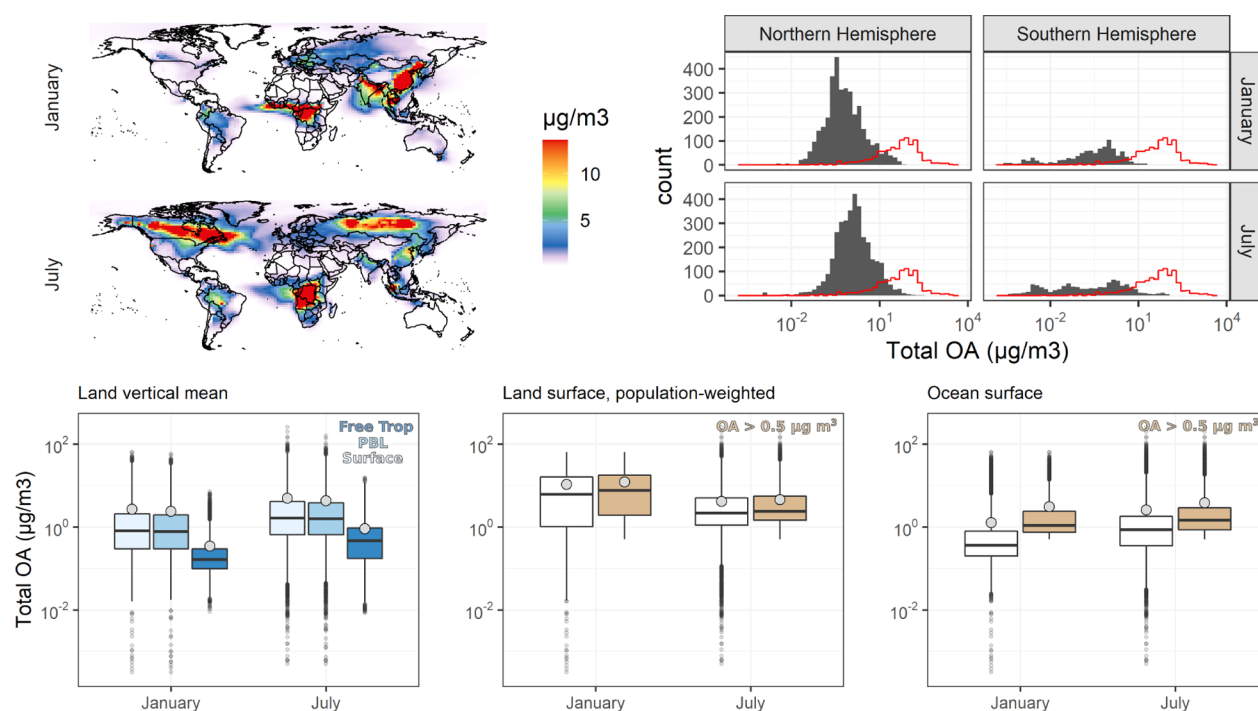


Figure 5. As with Figure 2, except for average monthly summed OA concentrations. Comparison distribution of mass loadings used in SOA chamber experiments indicated by the red line in histograms (upper right).

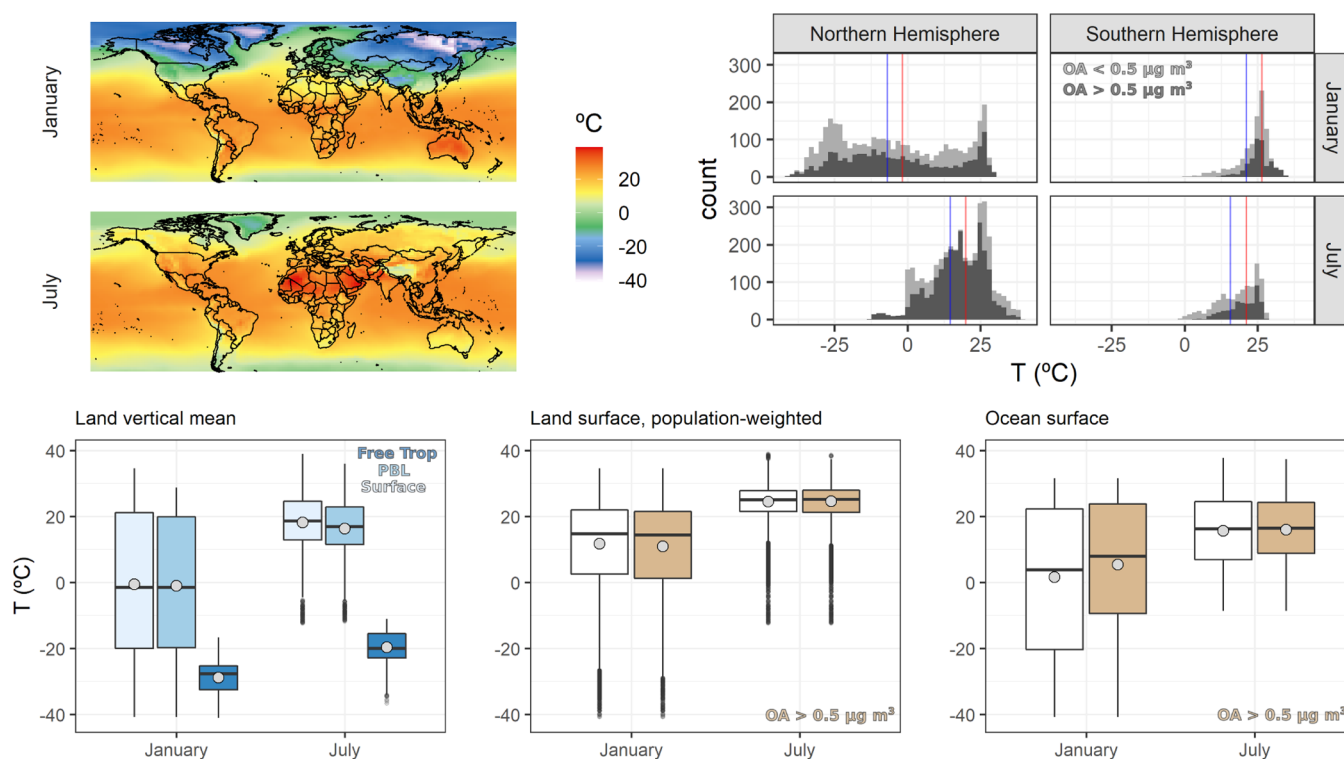


Figure 6. As with Figure 2, except for average monthly temperature.

RH is generally inversely correlated with temperature, as shown in the Figure 7 distributions. Land surfaces average just over 70% in January and around 66% in July, with most regions averaging over 50% RH in both seasons, though monthly means range from 15 to 100%. Population weighting condenses this global distribution to within the 50–80% range over both seasons.

While absolute humidity generally drops with elevation, average RH remains above 50% even in the free troposphere, due to the sharp reduction in temperature at higher altitudes. The differences between average daytime and average nighttime humidity over land (as shown by blue minima and red maxima, respectively, in Figure 7) range from 15 to 20%, illustrating clear diurnal cycles in RH. Masking RH

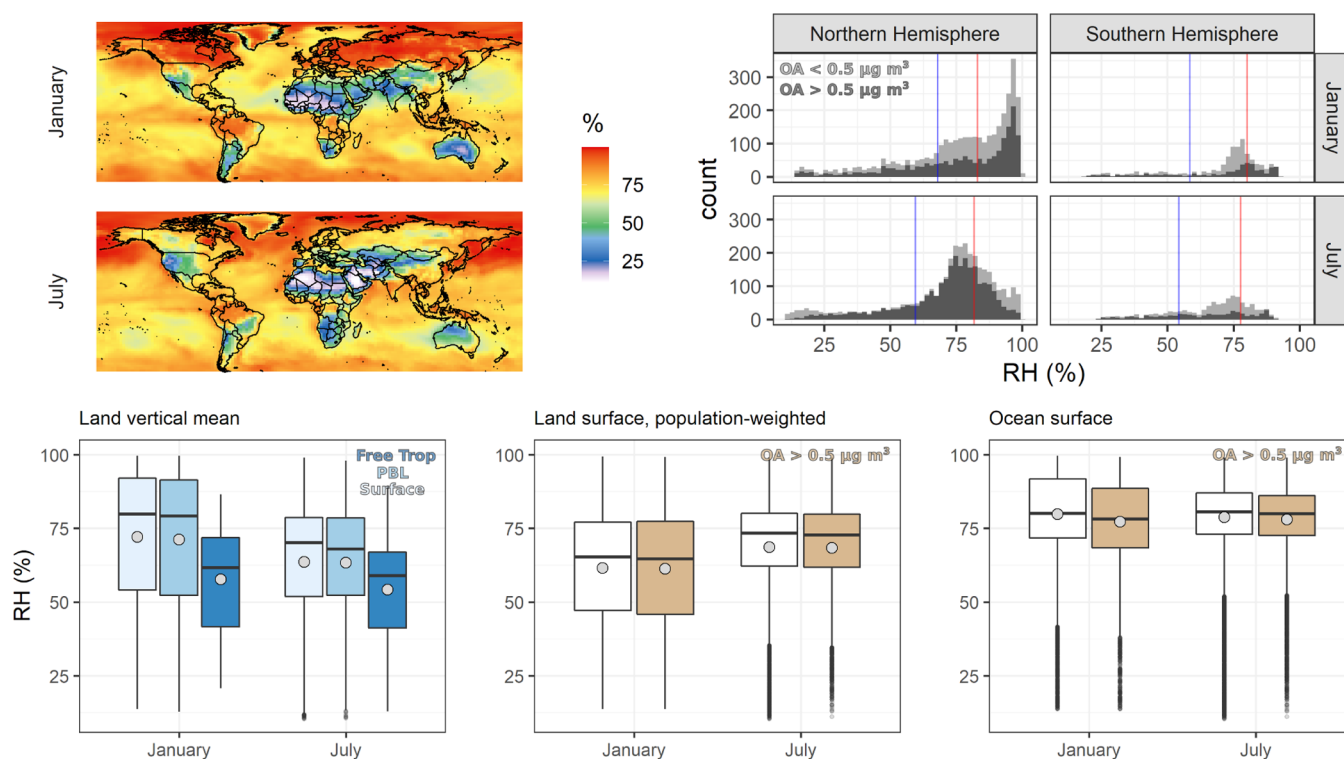


Figure 7. As with Figure 3, except for average monthly RH.

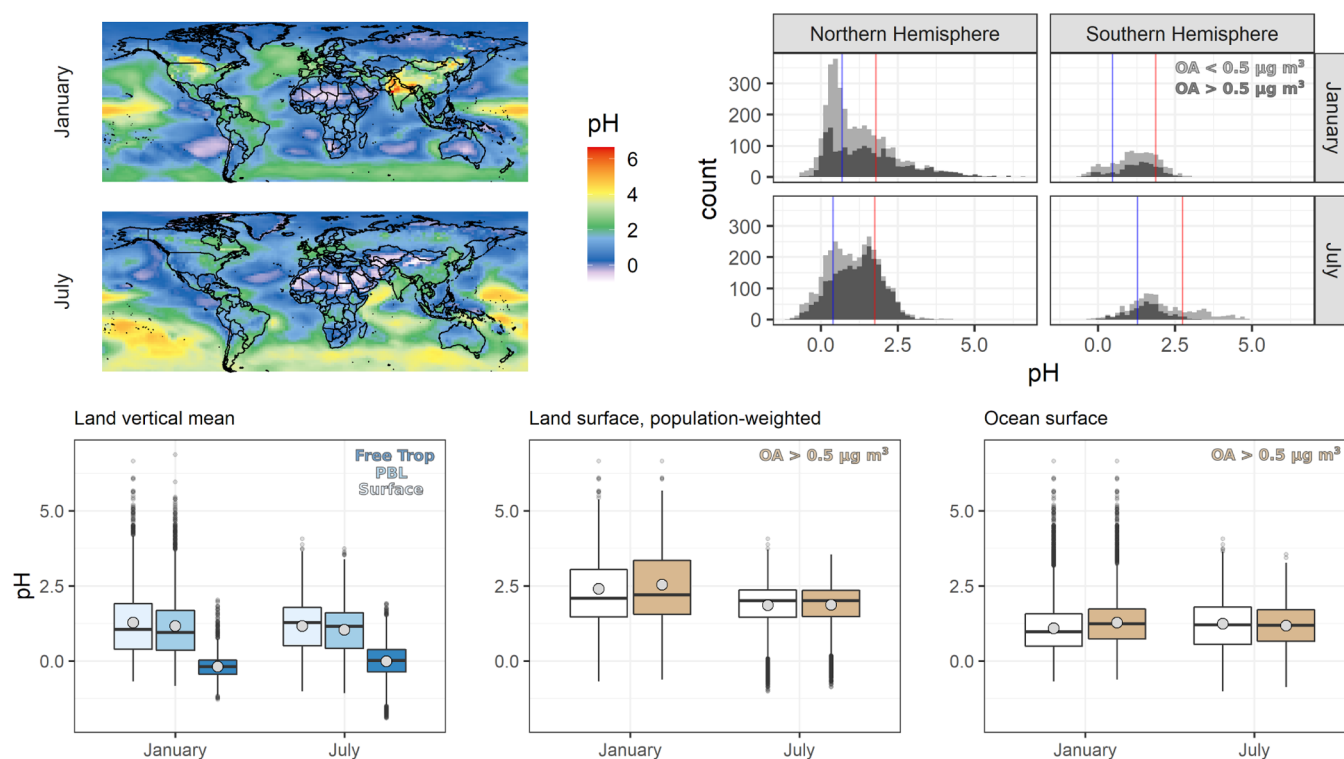


Figure 8. As with Figure 3, except for average monthly particle pH as calculated by ISORROPIA II.

distributions by grid cells with elevated OA concentrations has little impact on the distributions.

Particle LWC is a function of RH and particle composition. As described in the introduction and illustrated in Figure 1b,c, particle LWC affects gas/particle partitioning by modifying ζ and \overline{MW} ; pH and LWC and also affect multiphase reactions by

modifying the phase state, particle volume/surface area, and through catalysis. Distributions of modeled pH are stable across seasons, though a winter increase can be seen in some locations (Figure 8).

The modeled pH values are consistent with the relatively constant values of 0–2 reported by Weber et al.,⁷⁷ for regions

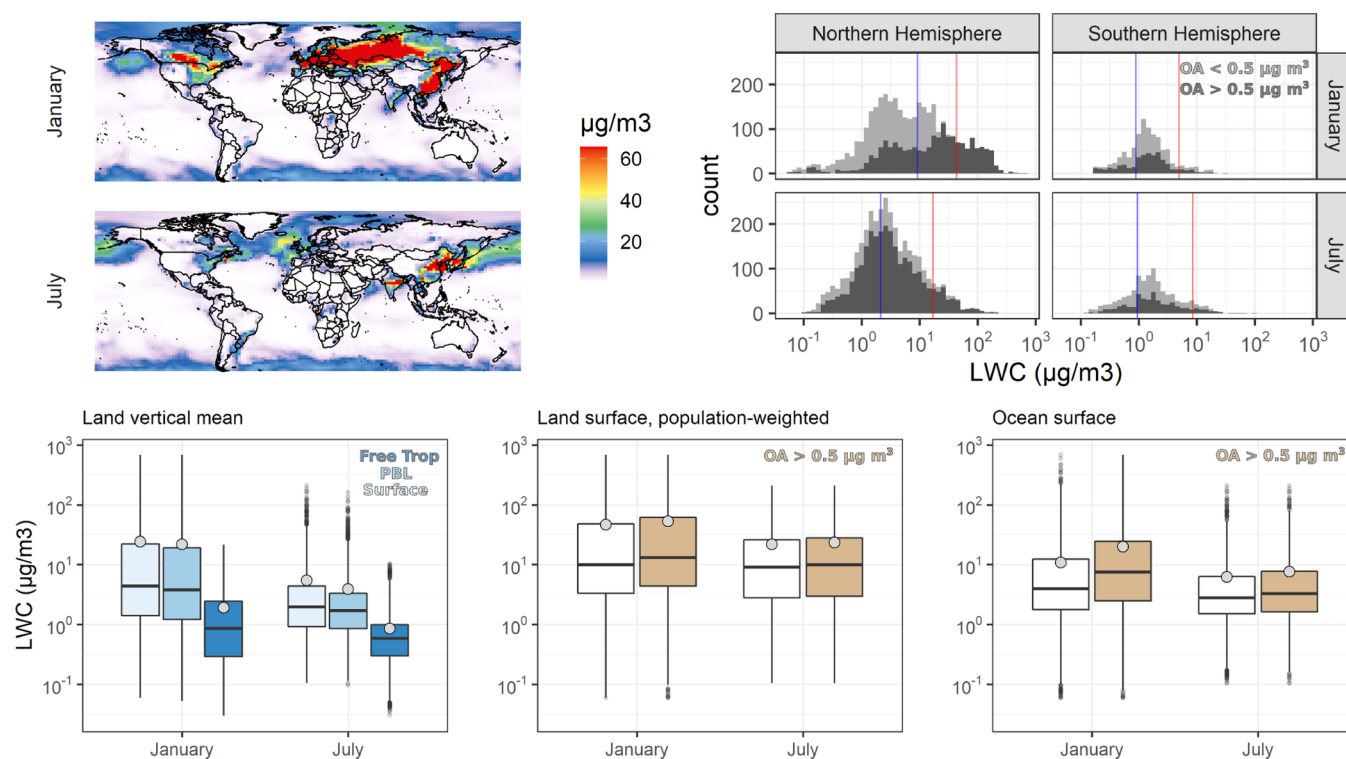


Figure 9. As with Figure 3, except for average monthly particle LWC as calculated by ISORROPIA II.

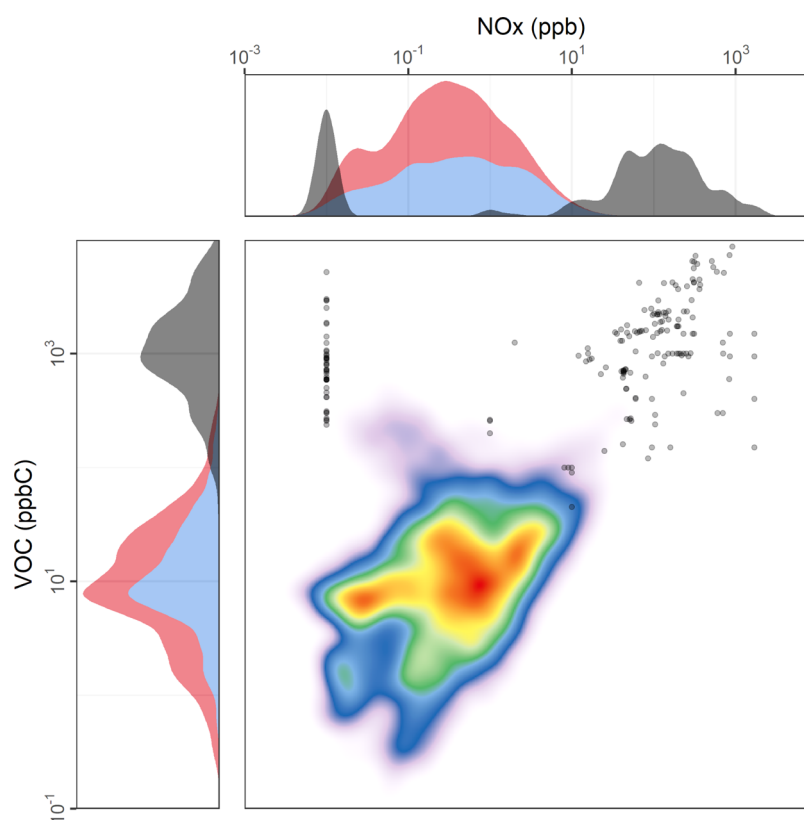


Figure 10. Two-dimensional (2D) heat map of the relative frequencies of NO_x (x -axis) and VOC (y -axis) mixing ratios, with season-specific marginal density distributions included above and to the left for January (blue distribution) and July (red distribution). NO_x and VOC levels reported in published SOA chamber experiments are shown as individual transparent points in the 2D plot, and their marginal distributions are represented in gray. Darker gray regions in the 2D scatter plot indicate individual overlapping points.

in which sulfate remains the dominant cation. Modeled LWC, on the other hand, shows strong seasonality and a heavy-tailed

distribution, which is especially pronounced in the northern mid-latitudes (Figure 9). Modeled LWC here is a lower-bound

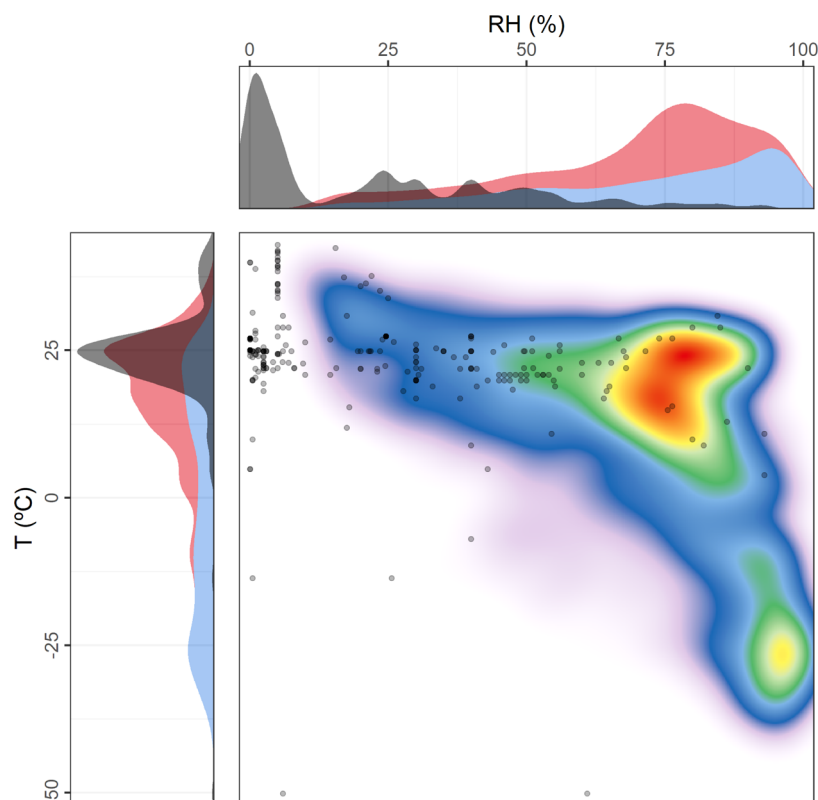


Figure 11. As with Figure 10, but for average monthly temperature and RH.

as water associated with organic compounds was not considered; underestimation is greatest where RH levels and the ratios of organic matter to organic carbon (OM/OC) are high, indicating a more polar condensed phase (e.g., Pye et al.⁷⁸). Based on summertime measurements in the Southeast US, where the averaged diurnal RH levels varied between ~50% and 90%, Guo et al.⁷⁹ estimated that 35% (and up to 50% at night) of total particle LWC was associated with the OA fraction. Pye et al.⁷⁸ demonstrated an increase in predicted SOA concentrations when water uptake by organic compounds and phase separation were considered, as well as an improvement in the model performance with the additional consideration of deviations from ideality.

The ratio of OM/OC describes the extent of oxygenation or functionalization of organic compounds in the condensed phase and is related to both precursor species and aging processes. Variability in OM/OC reflects differences in the polarity and solubility of the condensed compounds and can be linked to the particle-phase state and LWC. Aiken et al.⁸⁰ showed that observations of OM/OC and O/C were linearly correlated, with OM/OC ratios = 1.25 when O/C = 0 and OM/OC ratios = 2.44 when O/C = 1. The values of O/C, along with meteorological conditions such as T and RH, allow for prediction of the particle-phase state. Modeled OM/OC, phase state approximated by the ratio of the glass-transition temperature to the ambient temperature (T_g/T), separation RH (SRH), and phase separation approximated by the ratio of SRH to RH are shown in Figures S12–S15.

Laboratory-Model Comparison. The modeled parameter ranges can be compared with the laboratory distributions, as presented in Table S1, to identify gaps between existing chamber data and modeled ambient conditions. In the context of gas-phase chemistry, the VOC/ NO_x mixing ratio has often

been used as an indicator of the fate of RO_2 and the NO_x dependence of SOA yields in chamber studies.⁶ As shown in Figure 10, laboratory-based NO_x [ppb] and VOC [ppbC] mixing ratios were compared with model-predicted values. For studies in which NO_x values were reported as 0 or below the detection limit, a value of 0.01 ppb was assigned for illustration purposes; studies in which NO_x levels were not reported or could not be easily inferred, were not included in the figure. The gaps between modeled and experimental conditions for both VOC and NO_x mixing ratios shown are immediately apparent. VOC mixing ratios in typical chamber experiments are at times orders of magnitude above those predicted in the ambient atmosphere, again pointing to the differences in OA mass, as shown in Figure 5, with implications for SOA formation and yields, as described above. Model-predicted NO_x , on the other hand, sits squarely in between conditions most frequently used in chamber experiments. While this strategy of representing NO_x extremes through so-called “high NO_x ” and “low NO_x ” experiments is born out of practical considerations and is intended to focus on specific chemical pathways that can be added through some linear combination of partitioning parameters derived at those extremes, it leaves open the possibility of unrepresented mechanisms and products in the middle. The difficulty of exploring the space within this ambient chemical regime of lower VOCs and intermediate NO_x has led to this displacement in modeled versus measured VOC versus NO_x space, and it remains to be seen whether current or future measurements and/or modeling may help close these gaps.

As relevant for gas/particle partitioning and multiphase chemistry, grid counts of surface T and RH (Figure 11) peak between 20 and 30 °C and 70 to 80% RH in both January and July. The compilation of T and RH values from the laboratory

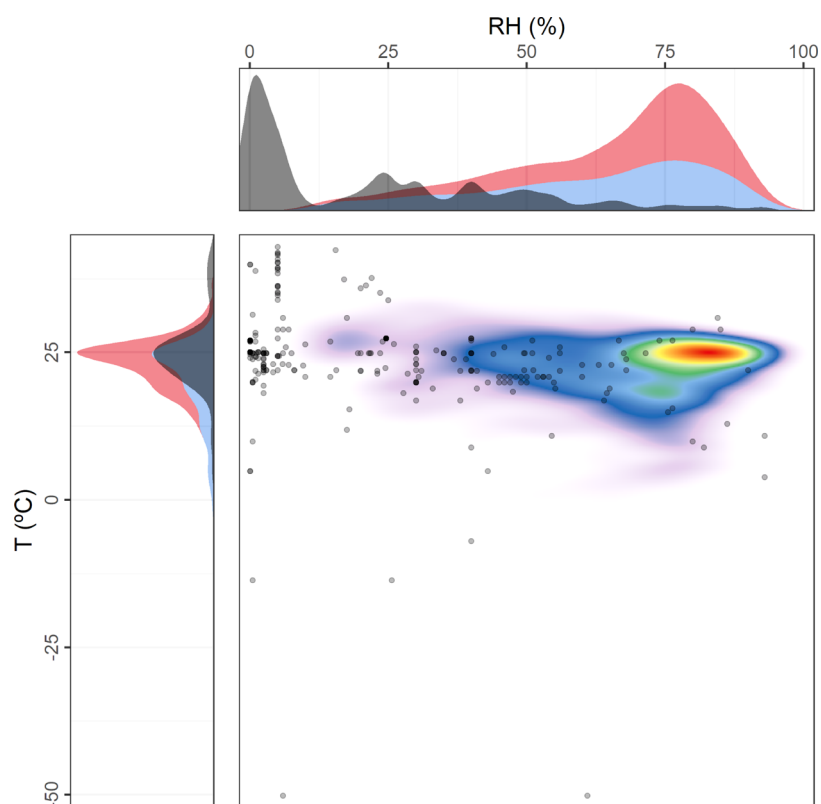


Figure 12. As with Figure 11, but restricted to grid cells identified as having higher SOA formation potential, defined as ≥ 75 th percentile for $[\text{RO}_2]/(\text{RO}_2 \text{ lifetime})$.

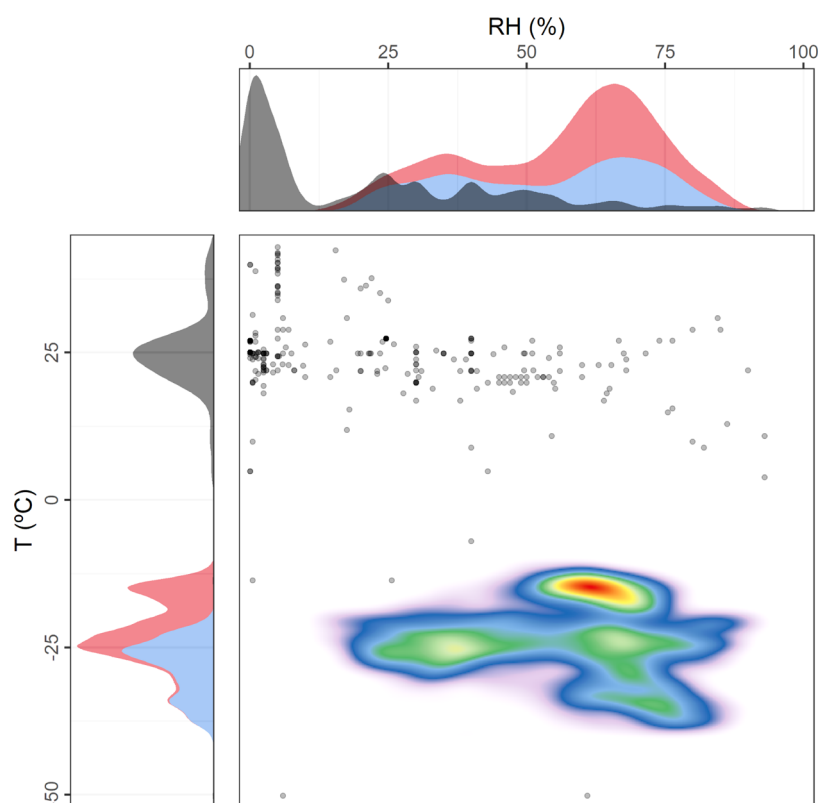


Figure 13. As with Figure 11, but for global free troposphere temperature and RH distributions. Grid cells limited to those with mean monthly RO_2 concentrations of ≥ 0.1 ppt.

studies shows relatively good overlap between the peaks of the surface temperature distributions and chamber conditions (Figure 11, left panel), with an underrepresentation below 20 °C. However, an evaluation of RH reveals distinct differences between surface distributions and those of published chamber studies (top panel). For practical measurement considerations, chamber studies have tended to favor dry air: over half of all experiments examined involved RH values less than 10%, and 89% used RH values less than 50%. A combination of these two distribution comparisons makes apparent the most significant gaps in terms of explored conditions in this T versus RH space: humid (greater than 70% RH) and cold winter conditions (less than 0 °C) are relatively common on the Earth's surface but have not seen commensurate representation in the published chamber literature. These significant differences between chamber RH and the ambient atmosphere suggest significant differences between the laboratory and ambient SOA in the context of composition (e.g., OM/OC and LWC) and phase state.

The grid counts of surface T and RH distributions were refined to better capture areas with higher SOA formation potential, defined by high RO_2 (i.e., indicator of SOA precursors) and low RO_2 lifetime (i.e., indicator of oxidants). Based on this metric, a threshold of inclusion was set at the 75th percentile. As shown in Figure 12, with this grid refinement, the temperature distributions largely overlap, suggesting that laboratory experiments generally capture surface conditions in those regions where SOA formation is most likely. However, the distinct differences in RH distributions between surface and chamber conditions persist. Conditions become increasingly disparate with vertical elevation, as shown in a similar figure (Figure 13) repeated for free troposphere locations and instead filtering by a minimum threshold of ≥ 0.1 ppt total RO_2 . While the precursors and conditions conducive to SOA formation are more likely found near the surface, cooling temperatures aloft can quickly shift conditions away from those represented in typical chamber experiments. These differences between chamber experiments and the ambient atmosphere have implications for derived SOA properties, as well as the partitioning parameters (i.e., C^*/K_p and α), used to predict SOA mass and composition in models.

Spatial differences in the representativeness of chamber conditions can be visualized by counting the number of studies using chamber T and RH values and comparing with modeled T and RH values at the surface. For each modeled grid cell, surveyed studies were filtered to count those whose chamber T and RH ranges overlapped even partially with the average diurnal cycle at that location. These tallies were computed across the modeled surface, producing a visualization of chamber representation—higher N values represent areas and seasons better represented by typical chamber study conditions, while lower values show areas and seasons that are more poorly represented (Figure 14). From these maps, it is apparent that in the context of T and RH, existing studies tend to represent July surface conditions in the mid-latitudes and tropics relatively well, along with January surface temperatures in the southern mid-latitudes and tropics. However, relatively few studies exist representing a variety of regions, in particular marine environments, boreal forests, wintertime northern mid-latitudes, and the Arctic.

Overlap between existing chamber data and modeled ambient conditions was further evaluated using two-dimen-

Study count: overlapping T and RH ranges

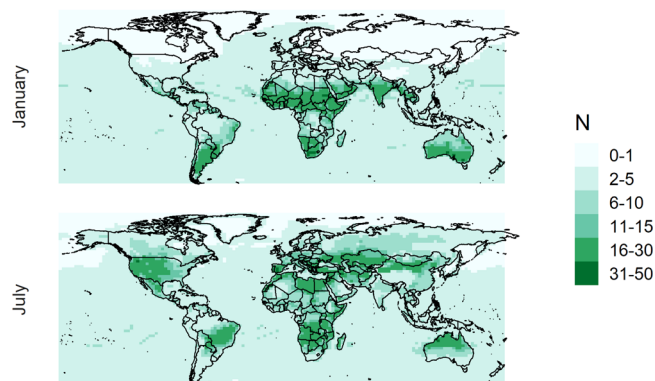


Figure 14. Number of laboratory studies whose temperature and RH values overlap with those of an average diurnal cycle for each surface grid cell. Higher mapped counts indicate regions better represented by typical chamber conditions.

sional comparisons between RH and OA mass (Figure 15). The paired comparison of RH and OA mass is relevant because mass loading affects the O/C ratio of the condensed phase and the volatility distribution of particle-phase compounds,^{81,82} with lower volatility (typically more oxidized) compounds having a greater contribution at lower mass loadings. Composition and RH levels control the LWC of the particles, which in turn influences gas/particle partitioning and multiphase chemistry (Figure 1). In the Figure 5 histogram, a red outline shows the total number of chamber experiments performed at various SOA mass loadings. The modeled ranges tend to fall well below the SOA mass loadings in the surveyed chamber studies, which are typically between 10 and 100 $\mu\text{g m}^{-3}$ (Figure 5, upper right). This gap between peaks (spanning roughly 2 orders of magnitude) illustrates one of the key differences between conditions representative of the ambient atmosphere and conditions in chamber experiments upon which model parameterizations are built. When RH and OA mass are considered concurrently (Figure 15), the gap between existing chamber data and atmospherically relevant conditions is even more stark, with chamber experiments occurring under much higher OA mass loadings and much lower RH conditions.

Developing SOA model parameterizations largely based on experimental chamber studies with RH values well below ambient values likely precludes accurate representation of processes that depend on RH and associated properties, such as particle LWC. Positive correlations between SOA yields and LWC have been observed for precursors including aromatics and terpenes, with higher SOA yields observed at higher LWC.⁸³ Higher RH, and more specifically, increased LWC can promote SOA formation by promoting the gas/particle partitioning of organic compounds [driven by an increase in m_{oa} and m_{T} ($m_{\text{oa}} + m_{\text{w}}$) and/or decrease in ζ]; some of which may then undergo particle-phase accretion reactions, further promoting SOA formation. However, not all laboratory studies have shown an influence of RH on the SOA yield,^{84,85} and the relationships between SOA yields, SOA composition, and RH are notably complex. The chemical composition of particles affects the extent to which particles absorb water in response to increasing RH; phase separation and particle morphology further influence the relationship between RH and LWC. If particles are phase separated and adopt a core-shell

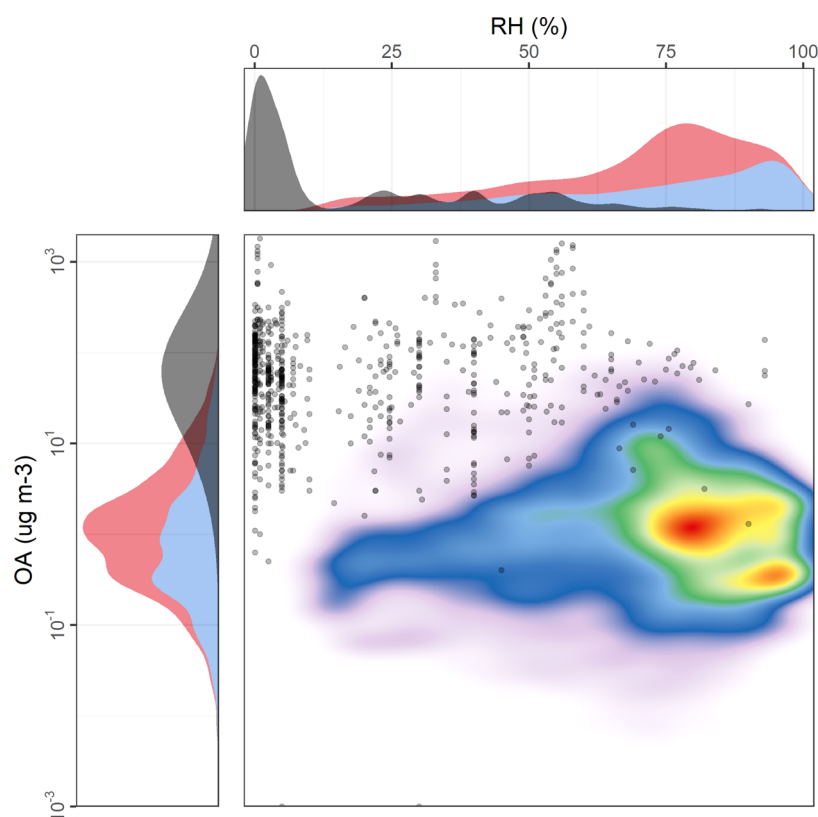


Figure 15. As with Figure 10, except for average monthly OA mass and RH.

morphology, in which an organic-rich phase surrounds a water-rich phase, RH and LWC may have a more limited effect on SOA formation.⁸⁶ Furthermore, when SOA formation is driven by reactions of stabilized Criegee intermediates (SCIs), at high RH SCIs are consumed in the gas phase, limiting their participation in accretion reactions and subsequently decreasing SOA yields, thereby resulting in a negative correlation between RH and SOA yields.⁸⁷

CONCLUSIONS

GEOS-Chem model output was used to survey 22 chemical and meteorological parameters, and associated derived properties, critical for predictions of SOA mass, composition, and physical properties, in an effort to quantitatively define atmospherically relevant ranges. The parameter ranges are summarized in Table 1, ordered by confidence in model outputs from high to low. Identifying parameters for which data under atmospherically relevant conditions are missing is important, given the reliance on such data for representations of SOA formation, composition, and properties in CTMs. Thus, for a subset of the parameters, comparisons were made between modeled values and laboratory data, based on a survey of 87 publications. For the subset of parameters analyzed, the most significant gaps were between chamber and modeled OA mass and RH, which has implications for modeled SOA mass, composition, and properties that are derived from chamber-based parameterizations. In order to improve model predictions of SOA mass and composition, additional laboratory-based studies are needed and, when not technically feasible, mechanistic-modeling studies, to close the gaps between chemical and meteorological conditions represented

by existing data and atmospherically relevant conditions based on model predictions, as surveyed and presented here.

ASSOCIATED CONTENT

Supporting Information

The Supporting Information is available free of charge at <https://pubs.acs.org/doi/10.1021/acsearthspacechem.1c00090>.

Model-Derived Parameter Calculations (PDF)

Supplementary Figures (PDF)

Laboratory Data (XLSX)

AUTHOR INFORMATION

Corresponding Author

Kelley C. Barsanti – Department of Chemical and Environmental Engineering and College of Engineering—Center for Environmental Research and Technology (CE-CERT), University of California Riverside, Riverside, California 92507, United States; orcid.org/0000-0002-6065-8643; Email: kbarsanti@engr.ucr.edu

Authors

William C. Porter – Department of Environmental Science, University of California Riverside, Riverside, California 92507, United States; orcid.org/0000-0002-3121-8323

Jose L. Jimenez – Department of Chemistry and Cooperative Institute for Research in Environmental Sciences (CIRES), University of Colorado, Boulder, Colorado 80309, United States; orcid.org/0000-0001-6203-1847

Complete contact information is available at:

<https://pubs.acs.org/doi/10.1021/acsearthspacechem.1c00090>

Author Contributions

The manuscript was conceptualized by K.C.B. and J.L.J. All authors contributed to selection and evaluation of parameters. W.C.P. conducted all of the GEOS-Chem model runs and generated all figures. The manuscript was written by K.C.B. and W.C.P., with input from J.L.J. All authors have given approval to the final version of the manuscript.

Notes

The authors declare no competing financial interest.

ACKNOWLEDGMENTS

K.C.B. acknowledges funding support from the NSF CAREER 1753364. J.L.J. acknowledges NSF AGS 1822664 for support. The authors thank Allan Bertram, Havala Pye, and Paul Ziemann for useful discussions regarding important parameters and Jia Jiang and Isaac Afreh for contributions to the Supporting Information laboratory data table.

REFERENCES

- (1) Zhang, Q.; Jimenez, J. L.; Canagaratna, M. R.; Allan, J. D.; Coe, H.; Ulbrich, I.; Alfarra, M. R.; Takami, A.; Middlebrook, A. M.; Sun, Y. L.; Dzepina, K.; Dunlea, E.; Docherty, K.; DeCarlo, P. F.; Salcedo, D.; Onasch, T.; Jayne, J. T.; Miyoshi, T.; Shimojo, A.; Hatakeyama, S.; Takegawa, N.; Kondo, Y.; Schneider, J.; Drewnick, F.; Borrmann, S.; Weimer, S.; Demerjian, K.; Williams, P.; Bower, K.; Bahreini, R.; Cottrell, L.; Griffin, R. J.; Rautiainen, J.; Sun, J. Y.; Zhang, Y. M.; Worsnop, D. R. Ubiquity and Dominance of Oxygenated Species in Organic Aerosols in Anthropogenically-Influenced Northern Hemisphere Midlatitudes. *Geophys. Res. Lett.* **2007**, *34*, L13801.
- (2) Barsanti, K. C.; Kroll, J. H.; Thornton, J. A. Formation of Low-Volatility Organic Compounds in the Atmosphere: Recent Advances and Insights. *J. Phys. Chem. Lett.* **2017**, *8*, 1503.
- (3) Ng, N. L.; Chhabra, P. S.; Chan, A. W. H.; Surratt, J. D.; Kroll, J. H.; Kwan, A. J.; McCabe, D. C.; Wennberg, P. O.; Sorooshian, A.; Murphy, S. M.; Dalleska, N. F.; Flagan, R. C.; Seinfeld, J. H. Effect of NO_x Level on Secondary Organic Aerosol (SOA) Formation from the Photooxidation of Terpenes. *Atmos. Chem. Phys.* **2007**, *7*, 5159–5174.
- (4) Ng, N. L.; Kroll, J. H.; Chan, A. W. H.; Chhabra, P. S.; Flagan, R. C.; Seinfeld, J. H. Secondary Organic Aerosol Formation from M-Xylene, Toluene, and Benzene. *Atmos. Chem. Phys.* **2007**, *7*, 3909–3922.
- (5) Song, C.; Na, K.; Cocker, D. R. Impact of the Hydrocarbon to NO_x Ratio on Secondary Organic Aerosol Formation. *Environ. Sci. Technol.* **2005**, *39*, 3143–3149.
- (6) Presto, A. A.; Huff Hartz, K. E.; Donahue, N. M. Secondary Organic Aerosol Production from Terpene Ozonolysis. 2. Effect of NO_x Concentration. *Environ. Sci. Technol.* **2005**, *39*, 7046–7054.
- (7) Chan, A. W. H.; Chan, M. N.; Surratt, J. D.; Chhabra, P. S.; Loza, C. L.; Crouse, J. D.; Yee, L. D.; Flagan, R. C.; Wennberg, P. O.; Seinfeld, J. H. Role of Aldehyde Chemistry and NO_x Concentrations in Secondary Organic Aerosol Formation. *Atmos. Chem. Phys.* **2010**, *10*, 7169–7188.
- (8) Surratt, J. D.; Chan, A. W. H.; Eddingsaas, N. C.; Chan, M.; Loza, C. L.; Kwan, A. J.; Hersey, S. P.; Flagan, R. C.; Wennberg, P. O.; Seinfeld, J. H.; Performed, S. P. H. Reactive Intermediates Revealed in Secondary Organic Aerosol Formation from Isoprene. *Proc. Natl. Acad. Sci. U.S.A.* **2010**, *107*, 6640.
- (9) Orlando, J. J.; Tyndall, G. S. Laboratory Studies of Organic Peroxy Radical Chemistry: An Overview with Emphasis on Recent Issues of Atmospheric Significance. *Chem. Soc. Rev.* **2012**, *41*, 6294–6317.
- (10) Bianchi, F.; Kurtén, T.; Riva, M.; Mohr, C.; Rissanen, M. P.; Roldin, P.; Berndt, T.; Crouse, J. D.; Wennberg, P. O.; Mentel, T. F.; Wildt, J.; Junninen, H.; Jokinen, T.; Kulmala, M.; Worsnop, D. R.; Thornton, J. A.; Donahue, N.; Kjaergaard, H. G.; Ehn, M. Highly Oxygenated Organic Molecules (HOM) from Gas-Phase Autoxidation Involving Peroxy Radicals: A Key Contributor to Atmospheric Aerosol. *Chem. Rev.* **2019**, *119*, 3472–3509.
- (11) Sato, K.; Hatakeyama, S.; Imamura, T. Secondary Organic Aerosol Formation during the Photooxidation of Toluene: NO_x Dependence of Chemical Composition. *J. Phys. Chem. A* **2007**, *111*, 9796–9808.
- (12) Henze, D. K.; Seinfeld, J. H.; Ng, N. L.; Kroll, J. H.; Fu, T.-M.; Jacob, D. J.; Heald, C. L. Global Modeling of Secondary Organic Aerosol Formation from Aromatic Hydrocarbons: High- vs. Low-Yield Pathways. *Atmos. Chem. Phys.* **2008**, *8*, 2405–2420.
- (13) Pye, H. O. T.; Chan, A. W. H.; Barkley, M. P.; Seinfeld, J. H. Global Modeling of Organic Aerosol: The Importance of Reactive Nitrogen (NO_x and NO₃). *Atmos. Chem. Phys.* **2010**, *10*, 11261–11276.
- (14) Carlton, A. G.; Bhawe, P. V.; Napelenok, S. L.; Edney, E. O.; Sarwar, G.; Pinder, R. W.; Pouliot, G. A.; Houyoux, M. Model Representation of Secondary Organic Aerosol in CMAQv4.7. *Environ. Sci. Technol.* **2010**, *44*, 8553–8560.
- (15) Teng, A. P.; Crouse, J. D.; Wennberg, P. O. Isoprene Peroxy Radical Dynamics. *J. Am. Chem. Soc.* **2017**, *139*, 5367–5377.
- (16) Xu, L.; Möller, K. H.; Crouse, J. D.; Otkjær, R. V.; Kjaergaard, H. G.; Wennberg, P. O. Unimolecular Reactions of Peroxy Radicals Formed in the Oxidation of α -Pinene and β -Pinene by Hydroxyl Radicals. *J. Phys. Chem. A* **2019**, *123*, 1661–1674.
- (17) Crouse, J. D.; Nielsen, L. B.; Jørgensen, S.; Kjaergaard, H. G.; Wennberg, P. O. Autoxidation of Organic Compounds in the Atmosphere. *J. Phys. Chem. Lett.* **2013**, *4*, 3513–3520.
- (18) Ehn, M.; Kleist, E.; Junninen, H.; Petäjä, T.; Lönn, G.; Schobesberger, S.; Dal Maso, M.; Trimborn, A.; Kulmala, M.; Worsnop, D. R.; Wahner, A.; Wildt, J.; Mentel, T. F. Gas Phase Formation of Extremely Oxidized Pinene Reaction Products in Chamber and Ambient Air. *Atmos. Chem. Phys.* **2012**, *12*, 5113–5127.
- (19) Tröstl, J.; Chuang, W. K.; Gordon, H.; Heinritzi, M.; Yan, C.; Molteni, U.; Ahlm, L.; Frege, C.; Bianchi, F.; Wagner, R.; Simon, M.; Lehtipalo, K.; Williamson, C.; Craven, J. S.; Duplissy, J.; Adamov, A.; Almeida, J.; Bernhammer, A.-K.; Breitenlechner, M.; Brilke, S.; Dias, A.; Ehrhart, S.; Flagan, R. C.; Franchin, A.; Fuchs, C.; Guida, R.; Gysel, M.; Hansel, A.; Hoyle, C. R.; Jokinen, T.; Junninen, H.; Kangasluoma, J.; Keskinen, H.; Kim, J.; Krapf, M.; Kürten, A.; Laaksonen, A.; Lawler, M.; Leiminger, M.; Mathot, S.; Möhler, O.; Nieminen, T.; Onnela, A.; Petäjä, T.; Piel, F. M.; Miettinen, P.; Rissanen, M. P.; Rondo, L.; Sarnela, N.; Schobesberger, S.; Sengupta, K.; Sipilä, M.; Smith, J. N.; Steiner, G.; Tomé, A.; Virtanen, A.; Wagner, A. C.; Weingartner, E.; Wimmer, D.; Winkler, P. M.; Ye, P.; Carslaw, K. S.; Curtius, J.; Dommen, J.; Kirkby, J.; Kulmala, M.; Riipinen, I.; Worsnop, D. R.; Donahue, N. M.; Baltensperger, U. The Role of Low-Volatility Organic Compounds in Initial Particle Growth in the Atmosphere. *Nature* **2016**, *533*, 527–531.
- (20) Zhao, Y.; Thornton, J. A.; Pye, H. O. T. Quantitative Constraints on Autoxidation and Dimer Formation from Direct Probing of Monoterpene-Derived Peroxy Radical Chemistry. *Proc. Natl. Acad. Sci. U.S.A.* **2018**, *115*, 12142–12147.
- (21) Donahue, N. M.; Robinson, A. L.; Stanier, C. O.; Pandis, S. N. Coupled Partitioning, Dilution, and Chemical Aging of Semivolatile Organics. *Environ. Sci. Technol.* **2006**, *40*, 2635–2643.
- (22) Pankow, J. F. An Absorption Model Of Gas/Particle Partitioning Of Organic Compounds In The Atmosphere. *Atmos. Environ.* **1994**, *28*, 185.
- (23) Chang, E. I.; Pankow, J. F. Prediction of Activity Coefficients in Liquid Aerosol Particles Containing Organic Compounds, Dissolved Inorganic Salts, and Water-Part 2: Consideration of Phase Separation Effects by an X-UNIFAC Model. *Atmos. Environ.* **2006**, *40*, 6422–6436.
- (24) Chang, E. I.; Pankow, J. F. Organic Particulate Matter Formation at Varying Relative Humidity Using Surrogate Secondary and Primary Organic Compounds with Activity Corrections in the Condensed Phase Obtained Using a Method Based on the Wilson Equation. *Atmos. Chem. Phys.* **2010**, *10*, 5475–5490.

- (25) Cappa, C. D.; Lovejoy, E. R.; Ravishankara, A. R. Evidence for Liquid-like and Nonideal Behavior of a Mixture of Organic Aerosol Components. *Proc. Natl. Acad. Sci. U.S.A.* **2008**, *105*, 18687–18691.
- (26) Bertram, A. K.; Martin, S. T.; Hanna, S. J.; Smith, M. L.; Bodsworth, A.; Chen, Q.; Kuwata, M.; Liu, A.; You, Y.; Zorn, S. R. Predicting the Relative Humidities of Liquid-Liquid Phase Separation, Efflorescence, and Deliquescence of Mixed Particles of Ammonium Sulfate, Organic Material, and Water Using the Organic-to-Sulfate Mass Ratio of the Particle and the Oxygen-to-Carbon Elemental Ratio of the Organic Component. *Atmos. Chem. Phys.* **2011**, *11*, 10995–11006.
- (27) Zuend, A.; Seinfeld, J. H. Modeling the Gas-Particle Partitioning of Secondary Organic Aerosol: The Importance of Liquid-Liquid Phase Separation. *Atmos. Chem. Phys.* **2012**, *12*, 3857–3882.
- (28) Virtanen, A.; Joutsensaari, J.; Koop, T.; Kannosto, J.; Yli-Pirilä, P.; Leskinen, J.; Mäkelä, J. M.; Holopainen, J. K.; Pöschl, U.; Kulmala, M.; Worsnop, D. R.; Laaksonen, A. An Amorphous Solid State of Biogenic Secondary Organic Aerosol Particles. *Nature* **2010**, *467*, 824–827.
- (29) Koop, T.; Bookhold, J.; Shiraiwa, M.; Pöschl, U. Glass Transition and Phase State of Organic Compounds: Dependency on Molecular Properties and Implications for Secondary Organic Aerosols in the Atmosphere. *Phys. Chem. Chem. Phys.* **2011**, *13*, 19238–19255.
- (30) Shiraiwa, M.; Seinfeld, J. H. Equilibration Timescale of Atmospheric Secondary Organic Aerosol Partitioning. *Geophys. Res. Lett.* **2012**, *39*, 2012GL054008.
- (31) Li, Y.; Shiraiwa, M. Timescales of Secondary Organic Aerosols to Reach Equilibrium at Various Temperatures and Relative Humidities. *Atmos. Chem. Phys.* **2019**, *19*, S959–S971.
- (32) Pankow, J. F. Gas/Particle Partitioning of Neutral and Ionizing Compounds to Single and Multi-Phase Aerosol Particles. 1. Unified Modeling Framework. *Atmos. Environ.* **2003**, *37*, 3323–3333.
- (33) Carlton, A. G.; Turpin, B. J. Particle Partitioning Potential of Organic Compounds Is Highest in the Eastern US and Driven by Anthropogenic Water. *Atmos. Chem. Phys.* **2013**, *13*, 10203–10214.
- (34) Surratt, J. D.; Murphy, S. M.; Kroll, J. H.; Ng, N. L.; Hildebrandt, L.; Sorooshian, A.; Szmigielski, R.; Vermeylen, R.; Maenhaut, W.; Claeys, M.; Flagan, R. C.; Seinfeld, J. H. Chemical Composition of Secondary Organic Aerosol Formed from the Photooxidation of Isoprene. *J. Phys. Chem. A* **2006**, *110*, 9665–9690.
- (35) Surratt, J. D.; Lewandowski, M.; Offenberg, J. H.; Jaoui, M.; Kleindienst, T. E.; Edney, E. O.; Seinfeld, J. H. Effect of Acidity on Secondary Organic Aerosol Formation from Isoprene. *Environ. Sci. Technol.* **2007**, *41*, 5363–5369.
- (36) Ervens, B.; Turpin, B. J.; Weber, R. J. Secondary Organic Aerosol Formation in Cloud Droplets and Aqueous Particles (AqSOA): A Review of Laboratory, Field and Model Studies. *Atmos. Chem. Phys.* **2011**, *11*, 11069–11102.
- (37) McNeill, V. F.; Woo, J. L.; Kim, D. D.; Schwier, A. N.; Wannell, N. J.; Sumner, A. J.; Barakat, J. M. Aqueous-Phase Secondary Organic Aerosol and Organosulfate Formation in Atmospheric Aerosols: A Modeling Study. *Environ. Sci. Technol.* **2012**, *46*, 8075–8081.
- (38) Odum, J. R.; Hoffmann, T.; Bowman, F.; Collins, D.; Flagan, R. C.; Seinfeld, J. H. Gas/Particle Partitioning and Secondary Organic Aerosol Yields. *Environ. Sci. Technol.* **1996**, *30*, 2580.
- (39) Barsanti, K. C.; Carlton, A. G.; Chung, S. H. Analyzing Experimental Data and Model Parameters: Implications for Predictions of SOA Using Chemical Transport Models. *Atmos. Chem. Phys.* **2013**, *13*, 12073.
- (40) Hoesly, R. M.; Smith, S. J.; Feng, L.; Klimont, Z.; Janssens-Maenhout, G.; Pitkanen, T.; Seibert, J. J.; Vu, L.; Andres, R. J.; Bolt, R. M.; Bond, T. C.; Dawidowski, L.; Kholod, N.; Kurokawa, J.-i.; Li, M.; Liu, L.; Lu, Z.; Moura, M. C. P.; O'Rourke, P. R.; Zhang, Q. Historical (1750–2014) Anthropogenic Emissions of Reactive Gases and Aerosols from the Community Emissions Data System (CEDS). *Geosci. Model Dev.* **2018**, *11*, 369–408.
- (41) Travis, K. R.; Jacob, D. J.; Fisher, J. A.; Kim, P. S.; Marais, E. A.; Zhu, L.; Yu, K.; Miller, C. C.; Yantosca, R. M.; Sulprizio, M. P.; Thompson, A. M.; Wennberg, P. O.; Crounse, J. D.; St. Clair, J. M.; Cohen, R. C.; Laughner, J. L.; Dibb, J. E.; Hall, S. R.; Ullmann, K.; Wolfe, G. M.; Pollack, I. B.; Peischl, J.; Neuman, J. A.; Zhou, X. Why Do Models Overestimate Surface Ozone in the Southeast United States? *Atmos. Chem. Phys.* **2016**, *16*, 13561–13577.
- (42) Van Donkelaar, A.; Martin, R. V.; Leaitch, W. R.; MacDonald, A. M.; Walker, T. W.; Streets, D. G.; Zhang, Q.; Dunlea, E. J.; Jimenez, J. L.; Dibb, J. E.; Huey, L. G.; Weber, R.; Andreae, M. O. Analysis of Aircraft and Satellite Measurements from the Intercontinental Chemical Transport Experiment (INTEX-B) to Quantify Long-Range Transport of East Asian Sulfur to Canada. *Atmos. Chem. Phys.* **2008**, *8*, 2999–3014.
- (43) Li, M.; Zhang, Q.; Streets, D. G.; He, K. B.; Cheng, Y. F.; Emmons, L. K.; Huo, H.; Kang, S. C.; Lu, Z.; Shao, M.; Su, H.; Yu, X.; Zhang, Y. Mapping Asian Anthropogenic Emissions of Non-Methane Volatile Organic Compounds to Multiple Chemical Mechanisms. *Atmos. Chem. Phys.* **2014**, *14*, 5617–5638.
- (44) Marais, E. A.; Wiedinmyer, C. Air Quality Impact of Diffuse and Inefficient Combustion Emissions in Africa (DICE-Africa). *Environ. Sci. Technol.* **2016**, *50*, 10739–10745.
- (45) Randerson, J. T.; Van Der Werf, G. R.; Giglio, L.; Collatz, G. J.; Kasibhatla, P. S. *Global Fire Emissions Database*, Version 4.1 (GFEDv4); ORNL Distributed Active Archive Center, 2017.10.3334/ORNLDAAC/1293.
- (46) Murray, L. T.; Jacob, D. J.; Logan, J. A.; Hudman, R. C.; Koshak, W. J. Optimized Regional and Interannual Variability of Lightning in a Global Chemical Transport Model Constrained by LIS/OTD Satellite Data. *J. Geophys. Res.: Atmos.* **2012**, *117*, 20307.
- (47) Guenther, A. B.; Jiang, X.; Heald, C. L.; Sakulyanontvittaya, T.; Duhl, T.; Emmons, L. K.; Wang, X. The Model of Emissions of Gases and Aerosols from Nature Version 2.1 (MEGAN2.1): An Extended and Updated Framework for Modeling Biogenic Emissions. *Geosci. Model Dev.* **2012**, *5*, 1471–1492.
- (48) Millet, D. B.; Guenther, A.; Siegel, D. A.; Nelson, N. B.; Singh, H. B.; De Gouw, J. A.; Warneke, C.; Williams, J.; Eerdekens, G.; Sinha, V.; Karl, T.; Flocke, F.; Apel, E.; Riemer, D. D.; Palmer, P. I.; Barkley, M. Global Atmospheric Budget of Acetaldehyde: 3-D Model Analysis and Constraints from in-Situ and Satellite Observations. *Atmos. Chem. Phys.* **2010**, *10*, 3405–3425.
- (49) Tai, A. P. K.; Mickley, L. J.; Heald, C. L.; Wu, S. Effect of CO₂ Inhibition on Biogenic Isoprene Emission: Implications for Air Quality under 2000 to 2050 Changes in Climate, Vegetation, and Land Use. *Geophys. Res. Lett.* **2013**, *40*, 3479–3483.
- (50) Hudman, R. C.; Moore, N. E.; Mebust, A. K.; Martin, R. V.; Russell, A. R.; Valin, L. C.; Cohen, R. C. Steps towards a Mechanistic Model of Global Soil Nitric Oxide Emissions: Implementation and Space Based-Constraints. *Atmos. Chem. Phys.* **2012**, *12*, 7779–7795.
- (51) Breider, T. J.; Mickley, L. J.; Jacob, D. J.; Ge, C.; Wang, J.; Payer Sulprizio, M.; Croft, B.; Ridley, D. A.; McConnell, J. R.; Sharma, S.; Husain, L.; Dutkiewicz, V. A.; Eleftheriadis, K.; Skov, H.; Hopke, P. K. Multidecadal Trends in Aerosol Radiative Forcing over the Arctic: Contribution of Changes in Anthropogenic Aerosol to Arctic Warming since 1980. *J. Geophys. Res.: Atmos.* **2017**, *122*, 3573–3594.
- (52) Fischer, E. V.; Jacob, D. J.; Millet, D. B.; Yantosca, R. M.; Mao, J. The Role of the Ocean in the Global Atmospheric Budget of Acetone. *Geophys. Res. Lett.* **2012**, *39*, L01807.
- (53) Croft, B.; Wentworth, G. R.; Martin, R. V.; Leaitch, W. R.; Murphy, J. G.; Murphy, B. N.; Kodros, J. K.; Abbatt, J. P. D.; Pierce, J. R. Contribution of Arctic Seabird-Colony Ammonia to Atmospheric Particles and Cloud-Albedo Radiative Effect. *Nat. Commun.* **2016**, *7*, 1–10.
- (54) Damian, V.; Sandu, A.; Damian, M.; Potra, F.; Carmichael, G. R. The Kinetic Preprocessor KPP - A Software Environment for Solving Chemical Kinetics. *Comput. Chem. Eng.* **2002**, *26*, 1567–1579.
- (55) Fountoukis, C.; Nenes, A. ISORROPIAII: A Computationally Efficient Thermodynamic Equilibrium Model for K⁺-Ca²⁺-Mg²⁺-

NH₄⁺-Na⁺-SO₄²⁻-NO₃⁻-Cl-H₂O Aerosols. *Atmos. Chem. Phys.* **2007**, *7*, 4639–4659.

(56) Pye, H. O. T.; Liao, H.; Wu, S.; Mickley, L. J.; Jacob, D. J.; Henze, D. K.; Seinfeld, J. H. Effect of Changes in Climate and Emissions on Future Sulfate-Nitrate-Ammonium Aerosol Levels in the United States. *J. Geophys. Res.: Atmos.* **2009**, *114*, 1205.

(57) Marais, E. A.; Jacob, D. J.; Jimenez, J. L.; Campuzano-Jost, P.; Day, D. A.; Hu, W.; Krechmer, J.; Zhu, L.; Kim, P. S.; Miller, C. C.; Fisher, J. A.; Travis, K.; Yu, K.; Hanco, T. F.; Wolfe, G. M.; Arkinson, H. L.; Pye, H. O. T.; Froyd, K. D.; Liao, J.; McNeill, V. F. Aqueous-Phase Mechanism for Secondary Organic Aerosol Formation from Isoprene: Application to the Southeast United States and Co-Benefit of SO₂ Emission Controls. *Atmos. Chem. Phys.* **2016**, *16*, 1603–1618.

(58) Wesely, M. L. Parameterization of Surface Resistances to Gaseous Dry Deposition in Regional-Scale Numerical Models. *Atmos. Environ.* **1989**, *23*, 1293–1304.

(59) Zhang, L.; Gong, S.; Padro, J.; Barrie, L. A Size-Segregated Particle Dry Deposition Scheme for an Atmospheric Aerosol Module. *Atmos. Environ.* **2001**, *35*, 549–560.

(60) Liu, H.; Jacob, D. J.; Bey, I.; Yantosca, R. M. Constraints from ²¹⁰Pb and ⁷Be on Wet Deposition and Transport in a Global Three-Dimensional Chemical Tracer Model Driven by Assimilated Meteorological Fields. *J. Geophys. Res.: Atmos.* **2001**, *106*, 12109–12128.

(61) Amos, H. M.; Jacob, D. J.; Holmes, C. D.; Fisher, J. A.; Wang, Q.; Yantosca, R. M.; Corbitt, E. S.; Galarneau, E.; Rutter, A. P.; Gustin, M. S.; Steffen, A.; Schauer, J. J.; Graydon, J. A.; Louis, V. L. S.; Talbot, R. W.; Edgerton, E. S.; Zhang, Y.; Sunderland, E. M. Gas-Particle Partitioning of Atmospheric Hg(II) and Its Effect on Global Mercury Deposition. *Atmos. Chem. Phys.* **2012**, *12*, 591–603.

(62) Sander, R. Compilation of Henry's Law Constants (Version 4.0) for Water as Solvent. *Atmos. Chem. Phys.* **2015**, *15*, 4399–4981.

(63) Safieddine, S. A.; Heald, C. L. A Global Assessment of Dissolved Organic Carbon in Precipitation. *Geophys. Res. Lett.* **2017**, *44*, 11672–11681.

(64) Chen, X.; Hopke, P. K. A Chamber Study of Secondary Organic Aerosol Formation by Limonene Ozonolysis. *Indoor Air* **2010**, *20*, 320–328.

(65) Brégonzio-Rozier, L.; Siekmann, F.; Giorio, C.; Pangui, E.; Morales, S. B.; Temime-Roussel, B.; Gratien, A.; Michoud, V.; Ravier, S.; Cazaunau, M.; Tapparo, A.; Monod, A.; Doussin, J.-F. Gaseous Products and Secondary Organic Aerosol Formation during Long Term Oxidation of Isoprene and Methacrolein. *Atmos. Chem. Phys.* **2015**, *15*, 2953–2968.

(66) Bruns, E. A.; El Haddad, I.; Keller, A.; Klein, F.; Kumar, N. K.; Pieber, S. M.; Corbin, J. C.; Slowik, J. G.; Brune, W. H.; Baltensperger, U.; Prévôt, A. S. H. Inter-Comparison of Laboratory Smog Chamber and Flow Reactor Systems on Organic Aerosol Yield and Composition. *Atmos. Meas. Tech.* **2015**, *8*, 2315–2332.

(67) Liu, T.; Huang, D. D.; Li, Z.; Liu, Q.; Chan, M.; Chan, C. K. Comparison of Secondary Organic Aerosol Formation from Toluene on Initially Wet and Dry Ammonium Sulfate Particles at Moderate Relative Humidity. *Atmos. Chem. Phys.* **2018**, *18*, 5677–5689.

(68) Boyd, C. M.; Nah, T.; Xu, L.; Berkemeier, T.; Ng, N. L. Secondary Organic Aerosol (SOA) from Nitrate Radical Oxidation of Monoterpenes: Effects of Temperature, Dilution, and Humidity on Aerosol Formation, Mixing, and Evaporation. *Environ. Sci. Technol.* **2017**, *51*, 7831.

(69) Li, W.; Li, L.; Chen, C.-I.; Kacarab, M.; Peng, W.; Price, D.; Xu, J.; Cocker, D. R. Potential of Select Intermediate-Volatility Organic Compounds and Consumer Products for Secondary Organic Aerosol and Ozone Formation under Relevant Urban Conditions. *Atmos. Environ.* **2018**, *178*, 109–117.

(70) Hennigan, C. J.; Miracolo, M. A.; Engelhart, G. J.; May, A. A.; Presto, A. A.; Lee, T.; Sullivan, A. P.; McMeeking, G. R.; Coe, H.; Wold, C. E.; Hao, W.-M.; Gilman, J. B.; Kuster, W. C.; De Gouw, J.; Schichtel, B. A.; Collett, J. L.; Kreidenweis, S. M.; Robinson, A. L. Chemical and Physical Transformations of Organic Aerosol from the

Photo-Oxidation of Open Biomass Burning Emissions in an Environmental Chamber. *Atmos. Chem. Phys.* **2011**, *11*, 7669–7686.

(71) Tkacik, D. S.; Robinson, E. S.; Ahern, A.; Saleh, R.; Stockwell, C.; Veres, P.; Simpson, I. J.; Meinardi, S.; Blake, D. R.; Yokelson, R. J.; Presto, A. A.; Sullivan, R. C.; Donahue, N. M.; Robinson, A. L. A Dual-Chamber Method for Quantifying the Effects of Atmospheric Perturbations on Secondary Organic Aerosol Formation from Biomass Burning Emissions. *J. Geophys. Res.* **2017**, *122*, 6043–6058.

(72) Kurtén, T.; Rissanen, M. P.; Mackeprang, K.; Thornton, J. A.; Hyttinen, N.; Jørgensen, S.; Ehn, M.; Kjaergaard, H. G. Computational Study of Hydrogen Shifts and Ring-Opening Mechanisms in α -Pinene Ozonolysis Products. *J. Phys. Chem. A* **2015**, *119*, 11366–11375.

(73) Praske, E.; Otkjær, R. V.; Crouse, J. D.; Hethcox, J. C.; Stoltz, B. M.; Kjaergaard, H. G.; Wennberg, P. O.; Lester, M. I. Atmospheric Autoxidation Is Increasingly Important in Urban and Suburban North America. *Proc. Natl. Acad. Sci. U.S.A.* **2018**, *115*, 64.

(74) Spracklen, D. V.; Jimenez, J. L.; Carslaw, K. S.; Worsnop, D. R.; Evans, M. J.; Mann, G. W.; Zhang, Q.; Canagaratna, M. R.; Allan, J.; Coe, H.; McFiggans, G.; Rap, A.; Forster, P. Aerosol Mass Spectrometer Constraint on the Global Secondary Organic Aerosol Budget. *Atmos. Chem. Phys.* **2011**, *11*, 12109–12136.

(75) Tsigaridis, K.; Daskalakis, N.; Kanakidou, M.; Adams, P. J.; Artaxo, P.; Bahadur, R.; Balkanski, Y.; Bauer, S. E.; Bellouin, N.; Benedetti, A.; Bergman, T.; Berntsen, T. K.; Beukes, J. P.; Bian, H.; Carslaw, K. S.; Chin, M.; Curci, G.; Diehl, T.; Easter, R. C.; Ghan, S. J.; Gong, S. L.; Hodzic, A.; Hoyle, C. R.; Iversen, T.; Jathar, S.; Jimenez, J. L.; Kaiser, J. W.; Kirkevåg, A.; Koch, D.; Kokkola, H.; Lee, Y. H.; Lin, G.; Liu, X.; Luo, G.; Ma, X.; Mann, G. W.; Mihalopoulos, N.; Morcrette, J.-J.; Müller, J.-F.; Myhre, G.; Myriokefalitakis, S.; Ng, N. L.; O'Donnell, D.; Penner, J. E.; Pozzoli, L.; Pringle, K. J.; Russell, L. M.; Schulz, M.; Sciare, J.; Seland, Ø.; Shindell, D. T.; Sillman, S.; Skeie, R. B.; Spracklen, D.; Stavrou, T.; Steenrod, S. D.; Takemura, T.; Tiitta, P.; Tilmes, S.; Tost, H.; van Noije, T.; van Zyl, P. G.; von Salzen, K.; Yu, F.; Wang, Z.; Wang, Z.; Zaveri, R. A.; Zhang, H.; Zhang, K.; Zhang, Q.; Zhang, X. The AeroCom evaluation and intercomparison of organic aerosol in global models. *Atmos. Chem. Phys.* **2014**, *14*, 10845.

(76) Sheehan, P. E.; Bowman, F. M. Estimated Effects of Temperature on Secondary Organic Aerosol Concentrations. *Environ. Sci. Technol.* **2001**, *35*, 2129–2135.

(77) Weber, R. J.; Guo, H.; Russell, A. G.; Nenes, A. High Aerosol Acidity despite Declining Atmospheric Sulfate Concentrations over the Past 15 Years. *Nat. Geosci.* **2016**, *9*, 282–285.

(78) Pye, H. O. T.; Murphy, B. N.; Xu, L.; Ng, N. L.; Carlton, A. G.; Guo, H.; Weber, R.; Vasilakos, P.; Appel, K. W.; Budisulistiorini, S. H.; Surratt, J. D.; Nenes, A.; Hu, W.; Jimenez, J. L.; Isaacman-Vanwertz, G.; Misztal, P. K.; Goldstein, A. H. On the Implications of Aerosol Liquid Water and Phase Separation for Organic Aerosol Mass. *Atmos. Chem. Phys.* **2017**, *17*, 343–369.

(79) Guo, H.; Xu, L.; Bougiatioti, A.; Cerully, K. M.; Capps, S. L.; Hite, J. R.; Carlton, A. G.; Lee, S.-H.; Bergin, M. H.; Ng, N. L.; Nenes, A.; Weber, R. J. Fine-Particle Water and PH in the Southeastern United States. *Atmos. Chem. Phys.* **2015**, *15*, 5211–5228.

(80) Aiken, A. C.; Decarlo, P. F.; Kroll, J. H.; Worsnop, D. R.; Huffman, J. A.; Docherty, K. S.; Ulbrich, I. M.; Mohr, C.; Kimmel, J. R.; Sueper, D.; Sun, Y.; Zhang, Q.; Trimborn, A.; Northway, M.; Ziemann, P. J.; Canagaratna, M. R.; Onasch, T. B.; Alfarra, M. R.; Prevot, A. S. H.; Dommen, J.; Duplissy, J.; Metzger, A.; Baltensperger, U.; Jimenez, J. L. O/C and OM/OC Ratios of Primary, Secondary, and Ambient Organic Aerosols with High-Resolution Time-of-Flight Aerosol Mass Spectrometry. *Environ. Sci. Technol.* **2008**, *42*, 4478–4485.

(81) Shilling, J. E.; Chen, Q.; King, S. M.; Rosenoern, T.; Kroll, J. H.; Worsnop, D. R.; Aiken, A. C.; Sueper, D.; Jimenez, J. L.; Martin, S. T. Loading-Dependent Elemental Composition of α -Pinene SOA Particles. *Atmos. Chem. Phys.* **2009**, *9*, 771–782.

(82) Presto, A. A.; Donahue, N. M. Investigation of α -Pinene + Ozone Secondary Organic Aerosol Formation at Low Total Aerosol Mass. *Environ. Sci. Technol.* **2006**, *40*, 3536–3543.

(83) Faust, J. A.; Wong, J. P. S.; Lee, A. K. Y.; Abbatt, J. P. D. Role of Aerosol Liquid Water in Secondary Organic Aerosol Formation from Volatile Organic Compounds. *Environ. Sci. Technol.* **2017**, *51*, 1405–1413.

(84) Cocker, D. R.; Mader, B. T.; Kalberer, M.; Flagan, R. C.; Seinfeld, J. H. The Effect of Water on Gas-Particle Partitioning of Secondary Organic Aerosol: II. *m*-Xylene and 1,3,5-Trimethylbenzene Photooxidation Systems. *Atmos. Environ.* **2001**, *35*, 6073–6085.

(85) Prisle, N. L.; Engelhart, G. J.; Bilde, M.; Donahue, N. M. Humidity Influence on Gas-Particle Phase Partitioning of α -Pinene + O₃ Secondary Organic Aerosol. *Geophys. Res. Lett.* **2010**, *37*, L01802.

(86) Reid, J. P.; Bertram, A. K.; Topping, D. O.; Laskin, A.; Martin, S. T.; Petters, M. D.; Pope, F. D.; Rovelli, G. The Viscosity of Atmospherically Relevant Organic Particles. *Nat. Commun.* **2018**, *9*, 956.

(87) Zhao, Y.; Wingen, L. M.; Perraud, V.; Greaves, J.; Finlayson-Pitts, B. J. Role of the Reaction of Stabilized Criegee Intermediates with Peroxy Radicals in Particle Formation and Growth in Air. *Phys. Chem. Chem. Phys.* **2015**, *17*, 12500–12514.